UPPSALA
UNIVERSITET

Titanium-Based Negative Electrode Materials for Rechargeable Batteries

In Search of the Redox Reactions

TATIANA KORIUKINA

Dissertation presented at Uppsala University to be publicly examined in Sonja Lyttkens, Ångströmlaboratoriet, Lägerhyddsvägen 1, Uppsala, Thursday, 1 June 2023 at 09:00 for the degree of Doctor of Philosophy. The examination will be conducted in English. Faculty examiner: Professor Egbert Figgemeier (RWTH Aachen University, Aachen, Germany).

Abstract
Koriukina, T. 2023. Titanium-Based Negative Electrode Materials for Rechargeable Batteries. *In Search of the Redox Reactions*. *Digital Comprehensive Summaries of Uppsala Dissertations from the Faculty of Science and Technology* 2257. 75 pp. Uppsala: Acta Universitatis Upsaliensis. ISBN 978-91-513-1779-3.

Rechargeable batteries, particularly, lithium-ion batteries (LIBs) have proven to be stable and reliable energy storage devices over the past few decades. The rapid demands regarding battery applications and the pressure to move away from the fossil fuel era drive the search for new materials for better rechargeable batteries for electric vehicles, renewable energy storage, and portable electronics. In this context a deeper understanding of the electrochemical processes governing the electrochemical behaviour of batteries is required. This thesis work investigates the use of two titanium-based materials as negative electrode materials for lithium- and sodium-ion batteries. The focus is on identifying the redox reactions responsible for the electrochemical capacities observed for the materials. Having knowledge of the available redox reactions for new materials used in batteries is crucial in predicting whether they can compete with existing battery chemistries and be commercially viable.

One part of this thesis work examines the electrochemical behaviuor of a 2D titanium carbide, $Ti_3C_2T_x$, a member of the MXene family, in lithium- and sodium-ion batteries. The other part explores an *A*-site cation deficient $Li_{0.18}Sr_{0.66}Ti_{0.5}Nb_{0.5}O_3$ (L018STN) perovskite oxide, known for its high lithium-ion conductivity, in LIBs. The electrodes were electrochemically evaluated in pouch-cell batteries and analysed post hoc by means of X-ray photoelectron spectroscopy and X-ray absorption spectroscopy.

The results indicate that only the surface Ti(I), Ti(II), Ti(III), and Ti(IV) titanium species of the $Ti_3C_2T_x$ flakes participate in the redox reactions and give rise to the electrochemical capacity. Furthermore, the restacking of individual flakes within the bulk of the $Ti_3C_2T_x$ electrode limits the electroactive surface of a freestanding $Ti_3C_2T_x$ electrode that is available for the redox reactions. The reversible capacities of $Ti_3C_2T_x$ electrodes can be improved by long-term cycling (an effect known as capacity activation) and heat treatment, as the surface titanium species gradually oxidise to higher oxidation states, e.g., Ti(III) and Ti(IV), or transform to titanium oxides Ti_xO_y.

The results for L018STN electrodes show that both titanium and niobium are redox active on over-lithiation, that is, when more than one Li^+ was inserted per a vacant *A*-site. The structural reorganization during over-lithiation enabled access to diffusion paths for fast lithium-ion diffusion even when a high concentration of lithium was inserted into the structure.

The findings of this thesis work thus indicate that a portion of the $Ti_3C_2T_x$ electrode is electrochemically inactive when subjected to electrochemical cycling. This can be ascribed to its structure and two-dimensional nature. As a result, $Ti_3C_2T_x$ cannot outperform existing negative electrodes for lithium- or sodium-ion batteries. The results obtained for L018STN provide valuable information on the lithium-ion diffusion behaviours in *A*-site cation deficient perovskite oxides. In a broader sense, this thesis work emphasises the significance of employing a multi-technique approach to obtain a good understanding of the underlying redox mechanisms when analysing battery materials.

Keywords: Lithium-ion batteries, sodium-ion batteries, MXenes, perovskite oxides, redox reactions, XPS

Tatiana Koriukina, Department of Chemistry - Ångström, Structural Chemistry, Box 538, Uppsala University, SE-751 21 Uppsala, Sweden.

I knew well enough that one could fracture one's legs and arms and recover afterward, but I did not know that you could fracture the brain in your head and recover from that too.

Vincent van Gogh

List of papers

This thesis is based on the following papers, which are referred to in the text by their roman numerals.

I   Koriukina, T., Kotronia, A., Halim, J., Hahlin, M., Rosen, J., Edström, K., Nyholm, L. (2022) On the Use of $Ti_3C_2T_x$ MXene as a Negative Electrode Material for Lithium-Ion Batteries. *ACS Omega*, 7: 41696–41710

II   Koriukina, T., Ericson, T., Ihrfors, C., Halim, J., Rosen, J., Nyholm, L., Hahlin, M., Edström, K. The Activation Process of $Ti_3C_2T_x$ (MXene) Electrodes in Na-ion Rechargeable Batteries. *In manuscript*

III   Koriukina, T., Halim, J., Rosen, J., Edström, K., Nyholm, L., Hahlin, M. Improving $Ti_3C_2T_x$ (MXene) Capacity in Lithium-Ion Batteries Using Heat Treatment as an Alternative to Precycling. *In manuscript*

IV   Brant, W. R., Koriukina, T., Chien, Y.-C., Euchner, H., Sanz, J., Kuhn, A., Heinzmann, R., Indris, S., Schmid, S. Local structure transformations promoting high lithium diffusion in defect perovskite type structures *Electrochimica Acta*, 441: 141759

Reprints were made with permission from the publishers.

Comments on my contributions to the papers:

I. Took part in planning, performed all the characterisation measurements for the $Ti_3C_2T_x$ electrodes and interpreted data.Wrote the manuscript together with co-authors.

II. Took part in planning, performed all the characterisation measurements for the $Ti_3C_2T_x$ and TiO_2 electrodes and interpreted data.Wrote the manuscript with input from the co-authors.

III. Planned and performed all the characterisation measurements for the $Ti_3C_2T_x$ electrodes and interpreted data.Wrote the manuscript with input from the co-authors.

IV. Performed electrochemical and XPS measurements and took part in the interpretation of the results.Wrote parts of the manuscript.

Contents

Abbreviations

CC	Constant current
CMC	Carboxymethyl cellulose
CV	Cyclic voltammetry
DC	Direct current
DEC	Diethyl carbonate
EC	Ethyl carbonate
EIS	Electrochemical impedance spectroscopy
GITT	Galvanostatic intermittent titration technique
HAXPES	Hard X-ray photoelectron spectroscopy
ICI	Intermittent current interruption
Li018STN	$Li_{0.18}Sr_{0.66}Ti_{0.5}Nb_{0.5}O_3$
LIB	Lithium-ion battery
LLTO	$Li_{3x}La_{2/3x-x}\square_{1/3-2x}TiO_3$, where $\square$ is a vacancy
LSTN	$Li_{2y}Sr_{1-x-y}Ti_{1-2x}Nb_{2x}O_3$
NaFSI	Sodium bis(fluorosulfonyl)imide
NMP	N-methyl-2-pyrrolidone
OCP	Open-circuit potential
OCV	Open-circuit voltage
PFY	Partial fluorescent yield
PP	Polypropylene
PVDF	Polyvinylidene fluoride
RT	Room temperature
SIB	Sodium-ion battery
SEI	Solid electrolyte interphase
TEG-DME	Tetraethylene glycol dimethyl ether
TEY	Total electron yield
XANES	X-ray absorption near edge structure
XAS	X-ray absorption spectroscopy
XPS	X-ray photoelectron spectroscopy

1. Introduction

1.1 Lithium- and sodium-ion rechargeable batteries

In modern society, the demand for renewable sources of energy is increasing every year. This happens due to a variety of reasons, for example, in an attempt to slow down climate change and achieve the goals of the Paris Agreement (2016) [1], to decrease pollution of the environment associated with fossil fuel extraction or usage [2, 3], due to geopolitical reasons [4], etc. The main factor restricting humanity from switching to 100% renewable energy, besides the cost, is that the production of renewable energy is intermittent [3, 5]. Most of the time the peak of energy production does not match the peak of consumer usage, for instance, solar panels are producing energy during the day (or summer) and the need for electricity is considerably higher during the evening (or winter) when the sun is not shining. To be able to balance the grid, energy storage devices could be part of the solution [5, 6].

Rechargeable batteries, especially, lithium-ion batteries (LIBs) have emerged as very stable and reliable energy storage devices within the past couple of decades. We can find them in our smartphones, laptops, cordless vacuum cleaners, electric bikes, scooters, and cars. LIBs have made us more mobile and they succeeded in this by being quite high energy density energy storage devices. The fact that the development of LIBs was awarded the Nobel prize in chemistry in 2019 only underlines the importance of this invention [7].

Of course, there are a lot of desirable qualities one wishes the perfect battery to have. For example, a truly high energy density, a greener process of production, an ability to recycle end-of-life batteries, short charging times, a low risk of thermal runaway, a long cycle life, a low cost and ethical means of production are some of the most important. Clearly, it is quite challenging to meet all of these requirements within one system, hence sadly the perfect battery has still not been invented [8, 9]. On the other hand, battery applications also vary, influencing what kind of battery requirements will be the most essential. A car battery, for example, should be light and compact which is synonymous with a high volumetric energy density, while in the case of energy produced by a solar panel or a wind turbine, which relies on stationary batteries, the battery's weight or volume will not be critical in the same way as the battery lifetime is the overarching need. For these types of applications lower volumetric energy storage devices could be used, an excellent example is sodium-ion batteries [5, 6].

To understand the driving force of battery research, it is important to understand the way lithium- or sodium-ion batteries work. Their operational principles are very similar. A typical LIB cell usually consists of two electrodes:

the negative and the positive electrodes (or electrodes with lower and higher lithium-ion insertion potentials), separated physically with a plastic separator soaked in the electrolyte, *Figure 1.1* [9, 10].
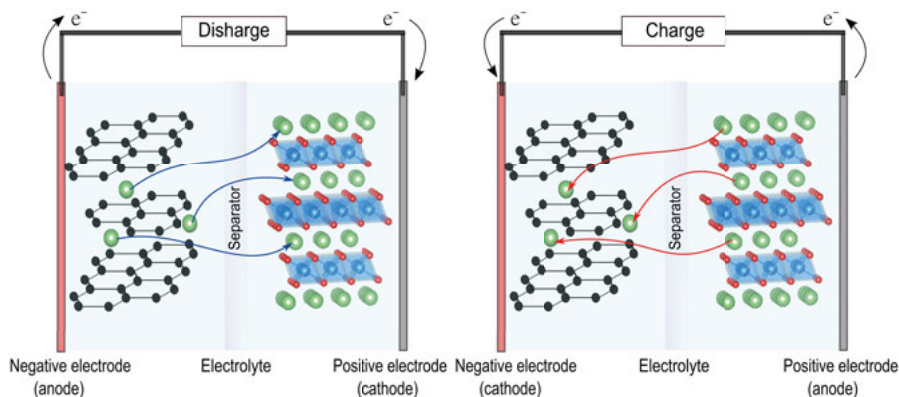

Figure 1.1. Operational principle of a typical LIB cell on discharge (left) and charge (right).

The electrolyte allows lithium ions to migrate and diffuse between the electrodes, while the separator prevents electrical contact between them which would otherwise result in short-circuiting of the cell. Typical "rocking chair" battery electrode materials operate via an intercalation (or insertion) mechanism, i.e., materials with a layered (or not) crystalline structure are used where lithium ions can be inserted and deinserted without causing significant distortions to the material's structure. On discharge, electrons are produced at the negative electrode (e.g., graphite composite electrode [10, 11]) during an oxidation reaction and these then move through the external circuit to the positive electrode (e.g., $LiCoO_2$ composite electrode [8, 9, 11]) where a reduction occurs. At the same time, lithium ions are deinserted from the negative electrode and travel through the electrolyte (e.g., 1 M $LiPF_6$ in an ethyl carbonate and diethyl carbonate (EC:DEC) 1:1 (v/v) solution) to get inserted into the positive electrode in order to maintain electroneutrality. On charge, the process is reversed. The total amount of charge that can be stored in a cell is called the capacity of the cell. The capacity of the cell is usually limited by the capacity of one of its electrodes, most often the positive electrode. To be able to compare different materials one often refers to a specific capacity: the capacity of the material per unit of mass. A common unit of specific capacity is thus mAh g^{-1} [11].

If the electrochemical reaction is known, one can calculate the specific capacity of the material through Faraday's law:

$$Q = \frac{nF}{3.6M} \qquad (1.1)$$

where Q is the specific capacity (mAh g^{-1}), n is the number of charge carriers, F is the Faraday's constant (96485.33 C/mol) and M is the molar mass of the host material. The energy density of a cell is the product of its specific capacity (or volumetric capacity) and cell voltage. Thus, there are two ways of increasing the energy density of a cell: by using electroactive materials with high specific (or volumetric) capacities or by combining materials that yield higher cell voltages.

Independent of the application, for a material to be a promising battery material, several requirements have to be fulfilled. First and foremost, a battery material has to undergo a reversible redox reaction involving the whole mass of the material. Secondly, such a reaction should take place within a suitable potential window (0 – 2.5 V for a material to be a negative electrode and 3.5 – 5 V for a material to be a positive electrode). Lastly, the material should show better performance or be produced in a cheaper, greener, or more ethical way to be able to outcompete already existing chemistries and be commercially attractive.

1.1.1 Negative electrode materials

Historically lithium metal was used as the first negative electrode in rechargeable lithium batteries [8, 11]. Lithium metal has undoubtedly the highest specific capacity for lithium storage, 3860 mAh g^{-1}, and the lowest standard potential, 0 V vs. Li$^+$/Li [11]. The main issue of using lithium metal in a cell is coupled to the lithium dendrite formation. The rough lithium metal surface leads to preferential growth of the lithium during repeated deposition on cycling and formation of needle-like structures, known as dendrites. Eventually, dendrites tend to reach the positive electrode causing short-circuiting of the battery, which in turn could lead to thermal runaway. Being aware of this hazard, the battery community moved to lithium metal-free batteries, LIBs.

In LIBs, scientists tend to distinguish between insertion, conversion, and alloying (negative) electrode materials based on the type of redox reaction happening on cycling [10].

Insertion materials
Insertion materials imply lithium ion insertion into their host structure without causing much structure distortion [10, 11]. If we are talking about crystalline materials, the term *topotactic transition* is also used, meaning that upon lithium-ion insertion the final structure is related to that of the original material by one or more crystallographically equivalent, orientational relationships [12]. The term *intercalation materials* is used when the structure of the negative electrode is layered, while for other structures (for instance, spinel structures) the term *insertion materials* is preferred. Disordered carbon material was the first commercialised insertion-type negative electrode (by Sony,

1991 [10, 11]). Graphite entered the market about five-six years later owing to the finding of an electrolyte that prevented graphite's exfoliation and allowed lithium-ion intercalation into the structure and continues to be one of the most common negative electrodes used commercially. The reason for this success is its high specific (gravimetric) capacity, 372 mAh g^{-1}, and relatively low lithium-ion intercalation potential of $\sim$0.2 V vs. Li$^+$/Li for the

$$C_6 + Li^+ + e^- = C_6Li \tag{1.2}$$

redox reaction [13–15]. Other insertion-type negative electrode materials are, for example, titanium dioxide, TiO$_2$, and lithium titanate, (Li$_4$Ti$_5$O$_{12}$, LTO). Their insertion potentials are higher than that of graphite and their specific capacities are lower in comparison with graphite. The insertion reaction for TiO$_2$ is

$$TiO_2 + x\,Li^+ + x\,e^- = Li_x TiO_2 \tag{1.3}$$
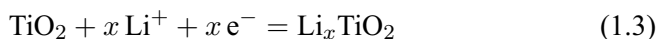
(where $0 < x < 1$). This insertion reaction takes place at $\sim$1.8 V vs. Li$^+$/Li, and involves a partial reduction of titanium ions from Ti(IV) to Ti(III) which yields a specific capacity of 168 mAh g^{-1} if $x = 0.5$ is assumed [16–18]. For LTO the insertion reaction is described as

$$Li_4Ti_5O_{12} + 3\,Li^+ + 3\,e^- = Li_7Ti_5O_{12} \tag{1.4}$$
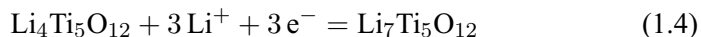
i.e., reduction of three titanium ions from Ti(IV) to Ti(III) and yields 175 mAh g^{-1} at $\sim$1.55 V vs. Li$^+$/Li [8, 11, 19]. The main advantage of TiO$_2$ and LTO negative electrodes is safety: higher insertion potential means no risk of lithium dendrite formation on cycling, while fast cycling usually promotes dendrite formation on the surface of graphite.

Conversion materials

Conversion materials involve conversion from one structure to another upon cycling, e.g., $Cu_2O + 2e^- + 2Li^+ = 2Cu + Li_2O$ [20, 21]. Some other examples of conversion materials are SnO$_2$, CuO, Fe$_2$O$_3$ [8, 21, 22]. The conversion materials have relatively high theoretical capacities (from 500 to 1500 mAh g^{-1}) but suffer from a low degree of reversibility, low lithium-ion mobility, and high volume expansion [20, 21].

Alloying materials

Alloying materials are those materials that form alloys with lithium, for example, Si, Al and Sn [8, 23, 24]. During the alloying reaction, lithium ions are reduced to lithium metal. One of the most attractive alloying materials is silicon. Its theoretical capacity is 3600 mAh g^{-1} and the alloying potential is 0.06 V vs. Li$^+$/Li. However, silicon's considerable volumetric expansion and shrinkage on cycling can cause crack formation, loss of the contact with current collector and continuous electrolyte degradation [8, 23, 24], which together with diffusion-controlled lithium trapping result in considerable capacity loss [25, 26] restricting commercial usage.

1.2 MXenes

MXenes (pronounced "Maxines") are a novel class of two-dimensional materials which has obtained its name from the fact that they are produced from MAX phases by etching away the A-metal. MAX phases are layered, hexagonal carbides and nitrides (space group $P6_3/mmc$) of the general formula: $M_{n+1}AX_n$, where n = 1 − 4, M is an early transition metal, A is an A-group (groups 13 and 14, e.g., Al or Si) element and X is either carbon and/or nitrogen [27]. MAX phases exhibit a combination of properties of metallic and ceramic materials and are known for their low density, low hardness, good machinability, high chemical resistance, and thermal and electrical conductivity [27–29].

MXenes in turn are 2D transitional metal carbides or nitrides, with the general formula $M_{n+1}X_nT_x$, where n = 1 − 4, and T is the termination group, coming from the synthesis (-OH, =O, -F or -Cl). An example of an -OH terminated $Ti_3C_2T_x$ MXene is depicted in *Figure 1.2C*. MXenes were discovered in 2011 by a graduate research student, Michael Naguib, under the supervision of Prof Michel Barsoum and Prof Yury Gogotsi, at Drexel University, Philadelphia, PA, USA [30, 31]. The synthesis that Naguib et. al. used is MAX phase etching in a fluoride-containing acidic water solution with subsequent delamination of accordion-shaped multilayered particles separated into 2D flakes via sonication, *Figure 1.2*. For the first reported MXene, $Ti_3C_2T_x$, Ti_3AlC_2 (prepared by ball-milling of Ti_2AlC and TiC) and 50% concentrated HF solution was used in the etching process [31].
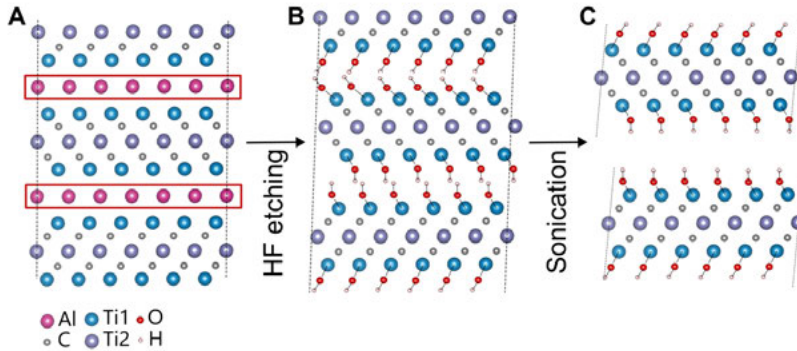

Figure 1.2. Schematic exfoliation process for Ti_3AlC_2. **A**: Ti_3AlC_2 structure. **B**: Al atoms replaced by OH after reaction with HF. **C**: Breakage of the hydrogen bonds and separation of $Ti_3C_2(OH)_2$ nanosheets. Adapted from [31].

Since there are 150 MAX phases reported to date [32], the discovery opened a door into a world of a whole family of new and exciting 2D materials.

Due to their structure, MXenes can have a unique combination of properties, including high electrical conductivity and mechanical properties (due to transition metal carbides/nitrides core); hydrophilicity (due to functionalised surfaces), as well as a high negative zeta-potential, enabling stable colloidal

solutions in water; efficient absorption of electromagnetic waves [33, 34] and even antibacterial [35] and antiviral properties [36, 37]. MXenes have been tested in various applications, including electrodes for lithium-ion [38–40], sodium-ion [41–43], potassium-ion [44–46] and Mg-ion batteries [47, 48], separators for lithium- [49], zinc-ion [50] and magnesium sulphur [51] batteries, current collectors for LIBs [52], supercapacitor electrodes [53–58], catalysts for heterogeneous catalysis [59, 60], hydrogen evolution reaction [59, 61] and other types of catalysis [59], as well as antennas for wireless communication [62, 63].

With time some more advanced synthesis routes for MXenes were found. Etching MAX phases in fluoride-containing water solution can be done not only with HF of different concentrations [38, 64], but also with in situ formed HF using a mixture of LiF and HCl [53, 64, 65] or with a mixture of HF and HCl [66, 67]. The optimised method of MAX phase etching in LiF and HCl solutions, referred to as MILD, facilitates single-flake manufacture and characterisation [68]. Alternatively, Li et al. [69] showed that the aluminium layer in Ti_3AlC_2T could be etched using a high-temperature hydrothermal approach in a NaOH solution. Electrochemical etching of MAX phases into MXenes in an ammonium chloride and tetramethylammonium hydroxide electrolyte was first demonstrated by Yang et al. [70]. The etching of MAX phases can also be water-free, Natu et al. [71] showed that it is possible to etch, and delaminate, MXenes in organic polar solvents (e.g., propylene carbonate, acetonitrile, dioxane. etc.) in the presence of ammonium dihydrogen fluoride, NH_4HF_2. Lastly, the possibility of etching MAX phases with Lewis acid molten salts, such as $ZnCl_2$ [72] or $CuCl_2$ [73] was also demonstrated. As a result of such a synthesis, MXenes uniformly terminated with Cl^- can be obtained.

The synthesis route was found to affect the morphology of MXene powders, for example, the most known accordion-like morphology is only observed when Ti_3AlC_2 is etched with concentrations of HF above 10% [42, 53, 64]. Some of the $Ti_3C_2T_x$ powder morphologies can be found in *Figure 1.3*.

A decade after the discovery there are at least 30 MXenes synthesised. Some examples are: Ti_2CT_x, Ti_2NT_x, V_2CT_x (n = 1); $Ti_3C_2T_x$, $(Ti,V)_2CT_x$ (n = 2); $Nb_4C_3T_x$, $Mo_2Ti_2C3T_x$ (n = 3); $(Mo,V)_5C_4T_x$ (n = 4) and $Mo_{1.33}CT_x$ (vacancy-containing i-MXene) [34, 74]. Despite this variety of MXenes that has been synthesised, in practice more than 70% of all the research on MXenes has been focused on the first discovered MXene, $Ti_3C_2T_x$ [34], the current work included. Several studies claim that the material could be used as a negative electrode for lithium-, sodium- and other beyond lithium-ion batteries. The specific capacity values that can be obtained for $Ti_3C_2T_x$, however, vary a lot in the literature [39, 75–77]. At the beginning of these research studies it was not certain if $Ti_3C_2T_x$ possesses an ability to be reduced or oxidised and if so, to which extent. In other words, the storage mechanism for the material in LIBs or beyond lithium-ion batteries was still a topic of discussion, and the redox reaction responsible for the observed capacity was yet to be revealed.
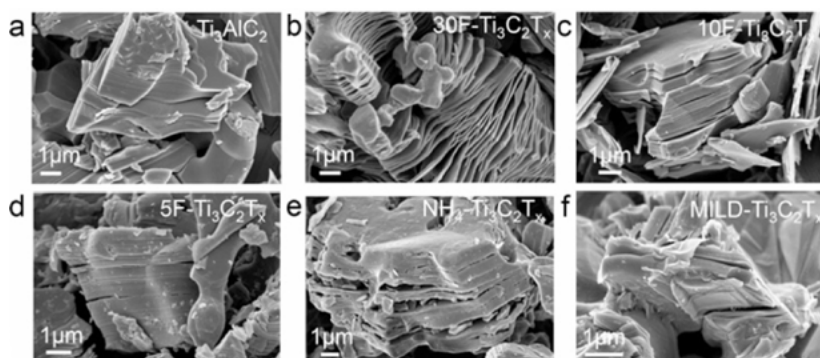
16

Figure 1.3. SEM images of (a) Ti_3AlC_2 (MAX) powder showing the compact layered structure and multilayered $Ti_3C_2T_x$ powder synthesised with (b) 30 wt %, (c) 10 wt %, and (d) 5 wt % HF. An accordion-like morphology was only observed for the 30 wt % HF etched powder (b). (e) Multilayered NH_4-$Ti_3C_2T_x$ powder synthesised with ammonium hydrogen fluoride and (f) MILD-$Ti_3C_2T_x$ powder etched with 10 M LiF in 9 M HCl, both showing the negligible opening of MXene lamellas, similar to what was observed in 5F-$Ti_3C_2T_x$. Reprinted with permission from [64]. Copyright 2023 American Chemical Society.

1.3 *A*-site cation deficient perovskite oxides

The structural family of perovskites comprises compounds having crystal structures related to the mineral perovskite $CaTiO_3$. This mineral was first discovered by the German mineralogist Gustav Rose in 1839 and was named in honour of the Russian mineralogist Lev Perovski (1792–1856) [78, 79]. Perovskite oxides are described by the general formula ABO_3, where large *A*-site cations fill the cuboctahedral cavities created by the three-dimensional network of corner linked BO_6 octahedra, *Figure 1.4*.
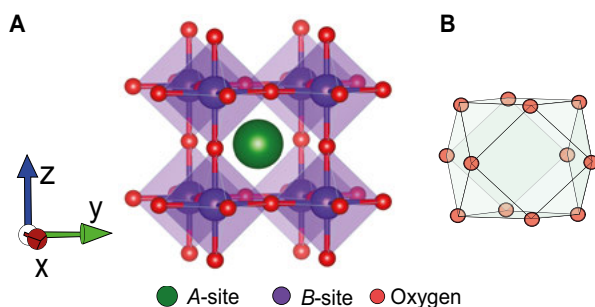

● *A*-site ● *B*-site ● Oxygen

Figure 1.4. **A**: Cubic crystal structure of perovskite oxide showing the coordination of the BO_6 octahedra. **B**: The vacant cuboctahedron AO_{12} (*A*-cage) formed from the corner linked BO_6 octahedra. The surface of the cuboctahedron consists of six O_4 square windows and eight O_3 triangular faces of the regular BO_6 octahedra [80].

Because of the large variety of A and B ions being compatible with the perovskite structure, this family of materials is huge. One of the most interesting features emerges when a vacancy on the A-site is introduced. Such a structure type is known as an A-site cation deficient perovskite oxides. The exclusion of A-site cations produces a vacant site large enough for small cation diffusion, depicted in *Figure 1.5*. This property led to the works on lithium lanthanum titanates, $Li_{3x}La_{2/3x-x}\square_{1/3-2x}TiO_3$ (where $\square$ is a vacancy) or LLTO, as solid-state ionic conductors. In 1987 Belous et al. first reported the stability and lithium-ion conduction behaviour of a perovskite-type LLTO [81] and in 1993 Inaguma et al. found that the bulk lithium-ion conductivity of LLTO could be as high as 10^{-3} S cm^{-1} at room temperature [82].

Since then numerous works have been performed exploring the origins of the high ionic conductivity and the possibility of using such deficient perovskite oxides as solid ionic conductors. However, it was later found that LLTO material has relatively lower ionic conductivity at grain boundaries (of the order of 10^{-5} S cm^{-1}) and inserts lithium ions in contact with metallic lithium [82–84]. The later discovery inspired works on using the material as an insertion electrode material for LIBs instead. Chen and Amine [85] were the first to demonstrate that it was possible to host significantly more than 1 Li$^+$ per available A-site cavity when LLTO was lithiated to 0 V vs. Li$^+$/Li. Specifically, $La_{0.55}Li_{0.35}TiO_3$ was able to reversibly insert 0.48 Li$^+$ per formula unit which corresponds to an average Li$^+$ A-site occupancy of 1.84. The concept of inserting more than one Li$^+$ per available A-site during lithiation in a LIB cell is going to be referred to as "over-lithiation" in this work. The concept can potentially explain the capacities that were previously observed for some of the A-site cation deficient perovskite oxides. For instance, it was recently reported that $Li_{1.5}La_{1.5}WO_6$ [86] shows a reversible capacity of $\sim$125 mAh g^{-1}, and that computational modelling predicts that up to 4 Li$^+$ can occupy a single A-site of $Li_{3.0}La_{1.5}WO_6$ during over-lithiation. A reversible capacity of $\sim$225 mAh g^{-1} was also reported for $La_{0.5}Li_{0.5}TiO_3$ at 1C rate for over 3000 cycles. While a portion of the capacity was suggested to arise from the intrinsic pseudocapacitance of the material, it demonstrates that a high concentration of lithium can be reversibly inserted into the structure [87].

The first attempts to explain the lithium-ion conductivity were based on the *site percolation* model. The idea is that lithium ions are hopping from one vacant A-site directly into an adjacent vacant A-site. In a cubic arrangement of vacant sites, significant diffusion only occurs if there are ≥ 0.34 vacant A-sites, see *Figure 1.5A*. According to this model, on average at least 2/6 O$_4$ windows in a cuboctahedron connect to another cuboctahedron that is vacant or contains a mobile cation, ensuring a continuous pathway. Furthermore, lithium-ion diffusion, in this case, is found to be reduced by the size of oxygen windows acting as bottlenecks between vacant sites [88, 89] and the strength of the Li-O bonding [90, 91].

The site-percolation model, however, appeared to be insufficient for describing lithium-ion mobility in perovskites adopting orthorhombic and rhombohedral symmetry, where lithium-ions are located in the centres of O_4 windows between the cuboctahedral A-site cavities. The *bond percolation* model was suggested instead [80, 92–94]. According to this model, the Li^+ diffusion pathways lie between the face centres of two adjacent O_4 windows. Therefore, for one Li^+ within the O_4 window, there are eight nearby sites in two adjacent A-site cavities into which it can move, four of these paths are shown in *Figure 1.5B*. It was also found that highly charged La^{3+} affects the lithium-ion diffusion paths: if O_4 sites are adjacent to La^{3+}, then lithium-ion diffusion through them is hindered [95]. This is why incorporating a cation with a lower charge should potentially improve the conduction properties of deficient perovskite oxides at higher lithium content. To this end, the $Li_{2y}Sr_{1-x-y}Ti_{1-2x}Nb_{2x}O_3$ (LSTN) family of compounds was investigated as an alternative, where La^{3+} ions are substituted with Sr^{2+}. Moreover, since Sr^{2+} has a larger ionic radius than La^{3+} (1.44 Å vs. 1.06 Å, respectively [90]), it creates larger A site cavities and presumably improves the conductivity [96]. Previous studies have also shown that Sr^{2+}-based deficient perovskite oxides tend to adopt cubic structures with a random distribution of entities occupying the A-site which leads to the formation of three-dimensional diffusion pathways [97, 98].
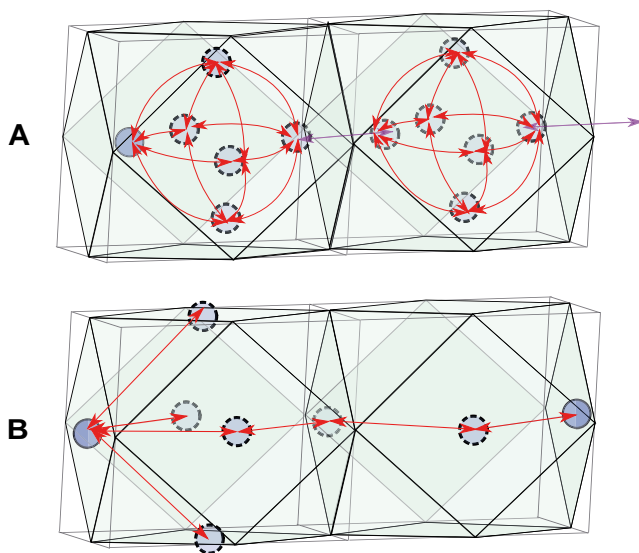

Figure 1.5. **A**: Site percolation mechanism involving lithium ions diffusion pathways between two cuboctahedra and **B**: Bond percolation mechanism involving lithium ions diffusion pathways between two cuboctahedra. In the latter case, all jump paths of the first lithium-ion are shown, and then only one possible conduction path is drawn thereafter. The oxygen atoms are not shown for clarity. Red arrows show fast lithium hopping paths and the purple arrows indicate relatively slower hopping paths.

2. Scope of the thesis

The scope of this thesis is to close the knowledge gap about the $Ti_3C_2T_x$ energy storage mechanism, explain the redox reactions possible for the $Ti_3C_2T_x$ in lithium- and sodium-ion batteries and evaluate if it is scientifically interesting to use this material as a negative electrode in these systems. **Paper I** is dedicated to revealing the redox reactions that are taking place upon $Ti_3C_2T_x$ cycling in a LIB cell and that are responsible for the observed reversible and irreversible capacities. In **Paper II** the phenomenon of electrochemical capacity activation upon $Ti_3C_2T_x$ cycling in sodium-ion (and partly in a LIB) cells is discussed, and the electrochemical performance of $Ti_3C_2T_x$ is compared to that of TiO_2 which is relatively well-studied. **Paper III** aims to improve the electrochemical performance of $Ti_3C_2T_x$ in LIB cells based on the knowledge gained from **Paper I** and **Paper II**.

Part of this thesis (**Paper IV**) is dedicated to studying the redox activity and structure transformations in another Ti-based battery material, the A-site cation deficient perovskite oxides oxide $Li_{0.18}Sr_{0.66}Ti_{0.5}Nb_{0.5}O_3$ (Li018STN), during over-lithiation. A-site cation deficient perovskite oxides are known for their high solid-state ion conductivity. However, the location of lithium ions in the structure, the lithium-ion diffusion mechanism, and the source of the observed reversible capacity are not yet fully understood when it comes to electrochemical cycling. **Paper IV** aims to understand the structural origins of the lithium-ion mobility behaviour in Li018STN during over-lithiation, i.e., when more than one lithium ion per A-site is inserted. In addition, the source of the observed reversible capacity, the diffusion paths available for lithium-ions upon cycling and how they are altered on over-lithiation are investigated.

3. Methods

3.1 Synthesis and electrode preparation

3.1.1 $Ti_3C_2T_x$ MXene

For this thesis work all the $Ti_3C_2T_x$ MXenes were obtained in a form of colloidal suspensions in deionised water that was synthesised by Dr Joseph Halim at Linköping University. In **Papers I** and **II** the suspensions came from a $Ti_3C_2T_x$-LiF synthesis, while in **Paper III** the electrochemical performances of $Ti_3C_2T_x$ MXene coming from two different syntheses, $Ti_3C_2T_x$-LiF and $Ti_3C_2T_x$-HF, were compared. The syntheses differ with respect to the etching agent used to etch the Al layers in the Ti_3AlC_2 MAX phase (the Ti_3AlC_2 synthesis is described in [99]). One utilises an HCl + LiF mixture, while the other uses an HCl + HF mixture. Both of the procedures are described below as well as in *Figure 3.1*.

$Ti_3C_2T_x$-LiF synthesis: to convert the Ti_3AlC_2 to $Ti_3C_2T_x$ flakes, 0.5 g of Ti_3AlC_2 powder was added to a premixed 10 ml aqueous solution of 12 M HCl (Fisher, technical grade) and 2.3 M LiF (Alfa Aesar, 98+%) in a Teflon bottle. Prior to adding the Ti_3AlC_2 powder to the HCl + LiF solution, this solution was placed in an ice bath. After adding the Ti_3AlC_2 powder, the whole mixture was kept in the ice bath for 30 minutes. This was done to avoid the initial overheating that can result from the exothermic nature of the aluminium etching reaction. The Teflon bottle was then placed on a magnetic stirrer hot plate in an oil bath and held at 35 °C for 24 hours. After the completion of the reaction, the mixture was washed three times with 40 ml of 1 M HCl to remove excess LiF, followed by three washings with 40 ml of 1 M LiCl (Alfa Aesar, 98+%). The mixture was subsequently repeatedly washed with 40 ml of distilled water until a dark black supernatant containing delaminated $Ti_3C_2T_x$ flakes was observed. The resulting suspension was then centrifuged for 20 minutes at 2000 rpm to produce the $Ti_3C_2T_x$ colloidal aqueous solution with a concentration of ~3.3 mg/mL. Further details regarding the synthesis can be found in the article published by Ghidiu et al. [53].

$Ti_3C_2T_x$-HF synthesis: 1 g of Ti_3AlC_2 powder was added to a mixture of 12 mL HCl (Fisher, 36.5%, Technical grade), 6 mL H_2O, and 2 mL HF (VWR Chemicals, 48%, AnalaR NORMAPUR® analytical reagent, Sweden), the concentration of HCl was 7.1 M and the concentration of HF 2.7 M, and the mixture was left stirring for 24 hours at 35 °C. Afterwards, the mixture was washed with deionised water through several cycles each of 40 mL, each time the mixture was centrifuged at 6000 rpm for 1 min followed by decanting
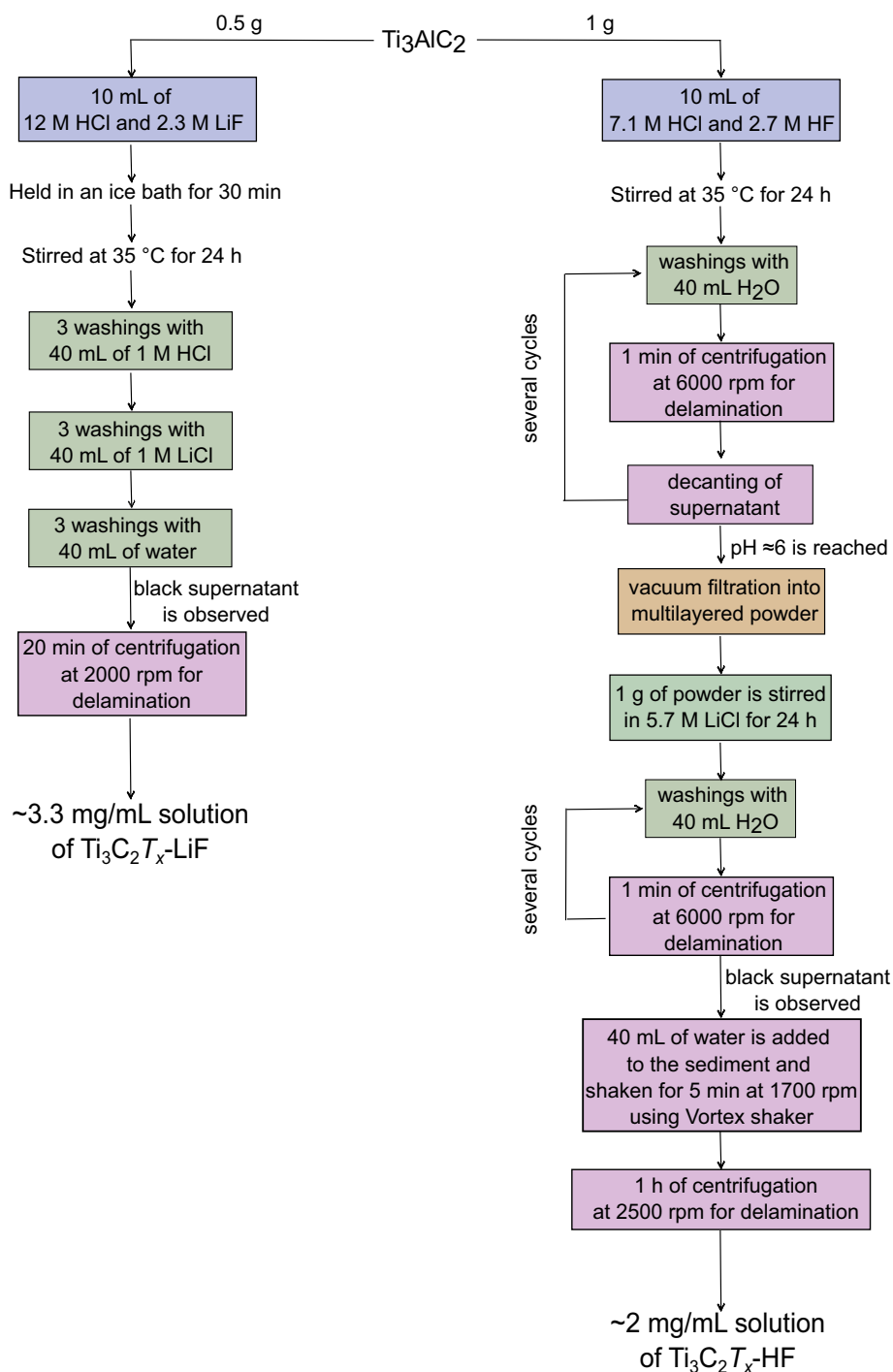
Figure 3.1. A schematic description of the $Ti_3C_2T_x$-LiF (left) and $Ti_3C_2T_x$-HF synthesis routes (right). The blue rectangles indicate the etching steps, the green rectangles indicate washings, the pink rectangles indicate the delamination steps, and the golden rectangle indicates the vacuum filtration step.

of the supernatant, the washing was done till the pH reached $\approx$6. After washing, the final mixture was vacuum filtered to obtain the multilayered powder and 1 g was then added to a 5.7 M LiCl solution (6 g of LiCl (Alfa Aesar, 98+%) dissolved in 25 mL of deionised water) and stirred for 24 hours at room temperature. For delamination, the mixture was washed with deionised water through several cycles each of 40 mL of water, the washing was stopped once a black supernatant was observed after centrifugation at 6000 rpm for 1 min. After that 40 mL of water was added to the sediment and was shaken for 5 min using the Vortex shaker (Sigma-Aldrich, CLS6776, Corning® LSE™) at 1700 rpm followed by centrifugation for 1 hour at 2500 rpm to obtain a supernatant of a colloidal suspension of single to few layers of $Ti_3C_2T_x$. The concentration of the obtained suspension was $\sim$2 mg/mL.

The $Ti_3C_2T_x$ suspensions were then sealed under argon in glass vials with a rubber septum and sent to Uppsala University. Since the $Ti_3C_2T_x$ suspensions are prone to oxidation, the manufacturing of the $Ti_3C_2T_x$ freestanding films was done within a week after puncturing a vial's septum with a syringe needle. After that, the vial was covered with a piece of parafilm to minimise the $Ti_3C_2T_x$ suspension exposure to air. About five millilitres of the suspension was vacuum filtrated through a 3501 Coated PP (polypropylene) Celgard membrane and left to dry in air to obtain a circular 45 mm in diameter and 5-7 µm thick $Ti_3C_2T_x$ MXene freestanding film. Freestanding electrodes were manufactured by punching the obtained films into circular electrodes with a diameter of either 7 mm and a mass loading of about 1.3 mg cm^{-2} or a diameter of 10 mm with a mass loading of about 1.7 mg cm^{-2}. The choice of the freestanding design for the electrodes was dictated by the idea of excluding the contributions from binders or conductive additives to the electrochemical cycling behaviours. In order to slow down the $Ti_3C_2T_x$ oxidation of the electrodes due to their contact with water and air, the electrodes were transferred into the glove box shortly after their manufacturing. Prior to the cell assembly, the electrodes were dried at 120 °C for 16 hours in a vacuum oven located in a glove box, if not stated otherwise.

3.1.2 TiO$_2$ nanotubes and nanoparticles

Amorphous $\sim$4.2 µm long TiO$_2$ nanotubes were manufactured through anodisation of a piece of titanium metal foil (0.125 mm thick, 99.6+% purity, Advent) of dimensions 1.5 cm × 1.5 cm in a two-electrode system as previously described [100–102]. The system comprised a platinum cathode, a titanium anode, an electrolyte consisting of 1 M NH$_4$F solution in 90 vol.% ethylene glycol (99.5% purity, <0.1 wt.% of H$_2$O) and 10 vol.% deionised water, as well as a DC power source (SM7020-D, Delta Elektronika). The anodisation of the titanium foil included two steps: 4-hour anodisation at 60 V and 30 min anodisation at 60 V. The obtained nanotube layer after the first anodisa-

tion step was removed by sonication in deionised water in order to expose the underlying textured titanium substrate. This textured substrate underwent the second anodisation step resulting in a morphologically more ordered structure. After the anodisation, the amorphous TiO_2 nanotube samples were rinsed in deionised water and dried in a flow of nitrogen.

Crystalline anatase TiO_2 nanotubes were prepared by annealing the amorphous TiO_2 nanotube samples. The annealing took place in air at 350 °C for 5 hours employing a heating rate of 6 °C min^{-1} starting at room temperature. After the annealing, the samples were left to cool down inside the furnace.

The obtained TiO_2 nanotube samples were then used as electrodes in sodium-ion cells. The TiO_2 nanotubes were standing on the titanium substrate. These electrodes were thus binder-free and were placed directly on an Al current collector.

TiO_2 nanoparticle composite electrodes were manufactured via doctor blade slurry casting on copper foil. The slurry contained 80 wt.% of 5 ± 1 nm sized crystalline anatase TiO_2 nanoparticles manufactured using a rapid hydrothermal route [103], 10 wt.% carboxymethyl cellulose binder (CMC-Na, d.s. 0.78, PA2000, Dow chemicals) and 10 wt.% carbon black (C-Nergy Super C65, Imerys Graphites & Carbon) dissolved in deionised water.

Before cell assembly, all the TiO_2 electrodes were dried at 120 °C for 5 hours in a vacuum oven located in a glove box.

3.1.3 *A*-site cation deficient perovskite oxide Li018STN

Polycrystalline samples of Li018STN were prepared by heating stoichiometric quantities of Li_2CO_3 (Merck, 99%), $SrCO_3$ (Aldrich, 99.9+%), TiO_2 (Aithaca, 99.995%) and Nb_2O_5 (Aithaca, 99.998 %) to 950 °C for 15 hours. The prepared pellets were heated at 1190 °C for 48 hours and then quenched in air. Electrodes for electrochemical cycling and X-ray photoelectron spectroscopy analysis were prepared by mixing L018STN, carbon black (Super C65, Imerys) and polyvinylidene fluoride (PVDF, Kynar PVDF HSV 900) in a 80:10:10 weight ratio with ~1 mL of N-methyl-2-pyrroli-done (NMP, ≥99.5%, GPR RECTAPUR) in a mixer mill to form a slurry. The slurry was then cast with a doctor blade casting machine onto a 20 µm thick copper foil with a 100 µm notch bar. In order to evaporate the NMP the cast electrode was kept at 70 °C for 2 hours and then at room temperature overnight. Electrodes of 13 mm diameter where then punched from the resulting coating. The active material mass loading of obtained electrodes varied between 5.5 and 6 mg cm^{-2}. Prior to the assembly, the composite electrodes were dried at 120 °C for 15 hours in a vacuum oven located in a glovebox.

24

3.2 Cell assembly and testing

The cells were assembled in argon-filled gloveboxes with oxygen and water contents < 1 ppm. The pouch cell two-electrode design was employed: the working electrode was separated from an 11 mm circular lithium or sodium metal foil combined reference and counter electrode with a circular 17 mm Celgard 2325 separator soaked in a 1 M $LiPF_6$ in 1:1 (v/v) EC:DEC solution or two of these separators soaked in a 1 molal sodium bis(fluorosulfonyl)imide (NaFSI) in a tetraethylene glycol dimethyl ether (TEG-DME) solution. When assembling a lithium half-cell, copper current collectors were used, while in the case of using sodium as a counter and reference electrode – aluminium current collectors were utilised. The cells were assembled mostly using pouch cell design, but in some cases, coin cells were used instead. Electrochemical cycling was performed on an Arbin BT-2043 Battery Test System and an MPG-2 battery tester.

Constant current (CC) cycling is electrochemical cycling that implies applying a constant current in order to charge and discharge a cell at a certain rate. The rate of cycling is usually expressed as the *C-rate*, where C is the current required to charge or discharge the full capacity of a cell within one hour. If the capacity of the material is unknown, a fixed value of charge/discharge current per unit of mass or unit of area is used instead. The technique is used for finding out the specific capacity and/or rate capability of an electrode material, as well as the coulombic efficiency during cycling. In the case of the negative electrode materials, the coulombic efficiency is defined as a ratio of the delithiation (oxidation) capacity to the lithiation (reduction) capacity for a chosen cycle. In this thesis, CC cycling is used to evaluate the reversible and irreversible specific capacities together with the coulombic efficiencies of $Ti_3C_2T_x$/Li, $Ti_3C_2T_x$/Na and Li018STN/Li cells during cycling.

Cyclic voltammetry (CV) is a technique that employs a discrete (staircase) sweep of the DC potential. One typically scans the potential window of interest with a certain scan rate to be able to track any redox reaction happening within this window. If a device is showing capacitive behaviour the response appears as a rectangle in the cyclic voltammogram. If there are reversible oxidation and reduction taking place, the cyclic voltammogram shows a pair (or multiple pairs) of reduction and oxidation peak(s). CV was used to reveal and identify the redox reactions taking place in $Ti_3C_2T_x$/Li, $Ti_3C_2T_x$/Na, TiO_2/Na and Li018STN/Li cells.

Intermittent current interruption (ICI) is a technique that is considered to be a fast alternative to the galvanostatic intermittent titration technique (GITT). ICI is usually coupled with CC, meaning that during the usual constant current cycling, a short pause in the applied current is introduced at regular intervals [104]. By analysing the potential change (ΔE) during the current interruption, an internal resistance (R), representing the sum of the electronic, ionic, and charge-transfer resistances, and a diffusion resistance coefficient (k), can be

obtained from the relationship:

$$\Delta E = -IR - Ik\sqrt{t} \tag{3.1}$$

where t is the time since the current was switched off. The diffusion resistance coefficient k is proportional to the coefficient of a Warburg element (σ) used in electrochemical impedance spectroscopy [105] and can be used to deduce the diffusion coefficient of lithium ions, $D_{Li}{}^+$, in an insertion electrode material according to a previously reported method [106]:

$$D_{Li^+} = \frac{4}{\pi} \left(\frac{V}{S} \frac{\frac{dE_{OC}}{dt_I}}{Ik} \right)^2 \tag{3.2}$$

where V is the molar volume, S is the electrochemically active surface area, $\frac{dE_{OC}}{dt_I}$ is the derivative of open-circuit potential (OCP) with respect to the time where the current is applied, which in the ICI method is approximated by the IR-drop corrected pseudo-OCP slope [106]. In some cases when the electrochemically active surface area of the sample is unknown a lithium-ion mobility ($m_{Li}{}^+ = D_{Li}{}^+ S^2 V^{-2}$) could be used instead. From equation 3.2 we get the expression for the lithium-ion mobility:

$$m_{Li^+} = \frac{4}{\pi} \left(\frac{\frac{dE_{OC}}{dt_I}}{Ik} \right)^2 \tag{3.3}$$

The ICI technique was used in **Paper IV** to track the internal resistance of the Li018STN/Li cell on CC cycling and observe the change in lithium-ion mobility within the Li018STN electrode during over-lithiation.

Electrochemical impedance spectroscopy (EIS) is a technique that is superimposing an oscillating electric potential of a small amplitude on a DC potential while the alternating current is measured. Impedance is thus the ratio between the alternating voltage and the alternating current. The data is usually presented in the form of a Nyquist plot, where the imaginary part of the impedance (Z") is plotted versus the real part of the impedance (Z'). Fitting EIS data to a meaningful equivalent circuit could be quite challenging since a good fit does not necessarily mean that chosen equivalent circuit has a physical meaning. EIS was used in **Paper II** to evaluate when charge transfer or diffusion was controlling the redox reaction seen for $Ti_3C_2T_x$ in $Ti_3C_2T_x$/Na cell and if the structure of freestanding $Ti_3C_2T_x$ MXene electrode was changed during cycling using two different cut-off potentials. EIS was also used in **Paper IV** to evaluate the ionic conductivity of a pristine Li018STN (pressed into a pellet and sintered) at room temperature. A two-electrode Swagelok cell with stainless steel blocking electrodes was used for this purpose.

3.3 Spectroscopic techniques

The depths of analysis of the spectroscopic techniques used in this thesis are schematically presented in comparison with the thickness of a sodiated or lithiated $Ti_3C_2T_x$ electrode in *Figure 3.2*. Such evaluations are rough estimations based on the mean free path of the electrons with specific kinetic energies [107–110].

X-ray photoelectron spectroscopy (XPS) is a technique used for surface analysis, typically the depth of probing is several nanometers. It is a photon-in – electron out technique, meaning that an X-ray source is used to produce photons which upon interaction with a sample are knocking out electrons from the atom's orbit. Electrons are then collected with an analyser and, by measuring the kinetic energy of these, one can extract their binding energy through the photoelectric effect equation:

$$E_B = h\nu - E_K - \phi \tag{3.4}$$

where E_B is the binding energy and E_K is the kinetic energy of the registered photoelectron, $h\nu$ is the incoming photon energy and ϕ is the work function of the instrument.
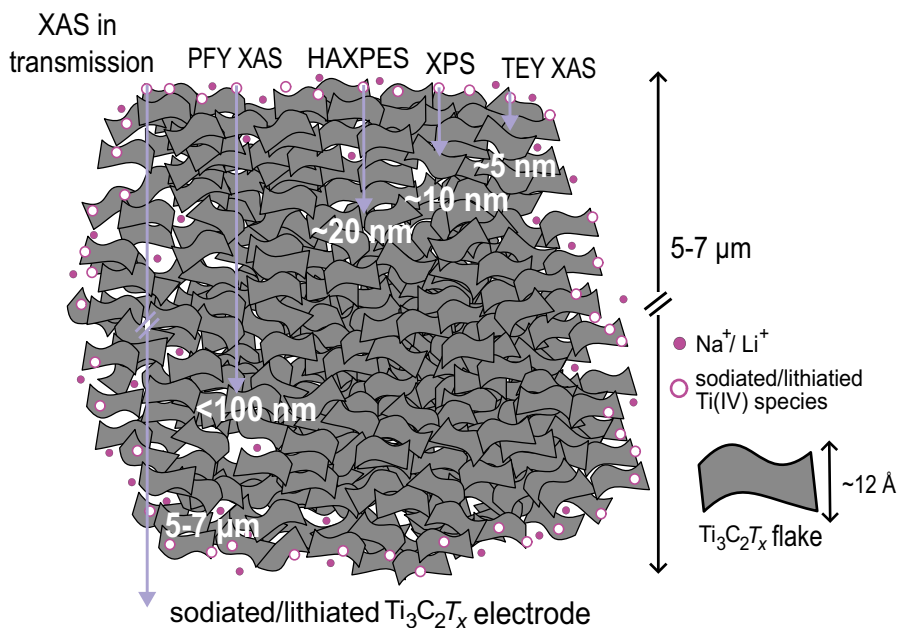

Figure 3.2. The depths of analysis of the used spectroscopic techniques in comparison with the thickness of a sodiated or lithiated $Ti_3C_2T_x$ freestanding electrode.

Based on binding energy, information about the elemental composition of the sample and the oxidation states of specific elements can be obtained. In this thesis, XPS was used to evaluate the oxidation state of titanium in $Ti_3C_2T_x$ and of both titanium and niobium in LSTN as well as to get information about species present on the surfaces of pristine, heat-treated, sodium-deposited or cycled $Ti_3C_2T_x$ electrodes. The XPS data was analysed with the CasaXPS software [111]. The binding energy calibration of the spectra was performed by referencing all the spectra to the C1s peak originating from the Ti-C peak located at 282.0 eV (**Papers I**, **II** and **III**), or to the C1s hydrocarbon peak at 284.8 eV (**Paper IV**). The ratio of the Ti-C peak area within the Ti2p region to the Ti-C peak area within the C1s region for $Ti_3C_2T_x$ was found to be relatively constant in **Paper I** and, was therefore, fixed to be constant in **Papers II** and **III**. The ratio between the areas of the 2p 1/2 Ti(IV) and 2p 1/2 Ti(III) peaks as well as between the areas of the 3d 5/2 Nb(V) and 3d 5/2 Nb(IV) peaks was used to evaluate the ratio between the Ti(IV) and Ti(III) species and between the Nb(V) and Nb(IV) species in $Li_{0.18+x}Sr_{0.66}Ti_{0.5}Nb_{0.5}O_3$ electrodes, respectively.

The in-house XPS data included in **Papers I** and **IV** was collected with a PHI-5500 instrument using Al-Kα radiation (1486.6 eV) and an electron emission angle of 45°, pass energy of 23.5 eV, a step size of 0.1 eV, and time per step of 100 mS. For the XPS data included in **Papers II** and **III**, a Kratos AXIS Supra$^+$ X-ray photoelectron spectrometer was used. A take-off angle of 90° with respect to the sample surface, pass energy of 20 eV, step size 0.1 eV was used for these XPS measurements. The beam-size was 700 × 300 μm. In **Paper II** a floating sample with charge neutralization was used, while in **Paper III** a sample was grounded during the measurements.

In **Paper III** in situ heating XPS measurements were also performed. The heating (and cooling) of the films was performed directly in the analyser chamber where the XPS measurements took place. The pressure in the analyser chamber was $\leq 6.7 \times 10^{-9}$ mbar prior to heating and stayed below 6.7×10^{-7} mbar during the measurements. The sample holder with the $Ti_3C_2T_x$ film screwed on was heated to a desired temperature and kept there for 5 minutes prior to measurement. The temperatures used in the in situ XPS heating experiments varied from room temperature to 775 °C.

Hard X-ray photoelectron spectroscopy (HAXPES) is a rather similar technique with the only difference being that it utilises higher photon energies in comparison with XPS and thus the probing depth is larger than that of XPS. The radiation sources used for HAXPES are typically silver or gallium anodes or synchrotrons. By combining data collected with XPS and HAXPES for the same sample one can obtain non-destructive elemental depth profiles. In this thesis, HAXPES was used to study the underlying surfaces of cycled or sodium deposited $Ti_3C_2T_x$ electrodes. The in-house HAXPES data in **Paper II** was collected with a Kratos AXIS Supra$^+$ X-ray photoelectron spectrometer using Ag-L$_\alpha$ radiation (2984.2 eV), a take-off angle of 90°, pass energy of 40 eV,

and a step size of 0.1 eV while the HAXPES data in **Paper I** was collected at the I09 beamline at the Diamond Light Source, Harwell, Oxfordshire, UK. In this case, a photon energy of 2.35 keV, pass energy of 70 eV, and a step size of 0.1 eV were used.

X-ray absorption spectroscopy (XAS) is yet another powerful spectroscopy technique that is allowing the identification of the electronic structure and the oxidation state of elements of interest. The technique is based on photon energy tuning when exciting the core-level electrons and probing the absorption edge of a specific element in the sample. Depending on the set-up, it could be either surface- or bulk-sensitive. In **Paper I** bulk sensitive XAS measurements on pristine and cycled $Ti_3C_2T_x$ electrodes in the transmission mode were performed at the BALDER beamline, MAX IV Laboratory, Lund, Sweden, while surface-sensitive XAS measurements with a total electron yield (TEY) detector were performed at the I09 beamline, Diamond Light Source, Harwell, Oxfordshire, UK. In **Paper II** the XAS data was collected for pristine and cycled $Ti_3C_2T_x$ electrodes with a TEY (sample drain current was used) and a partial fluorescent yield (PFY; Sirius 70 mm^2 active area SDD (Rayspec)) detectors at the FlexPES beamline at MAX IV Laboratory, Lund, Sweden. Since the TEY detector is more surface-sensitive than the PFY detector, one can obtain information about the oxidation state of titanium closer to the surface and deeper into the bulk of the $Ti_3C_2T_x$ electrodes. The X-ray Absorption Near Edge Structure (XANES) spectra were processed with the ATHENA software package [112], and E0 was found as the first peak of the first derivative of μ(E).

# 4. Results and discussion

4.1 $Ti_3C_2T_x$ MXene in lithium- and sodium-ion batteries

Attempts to produce new two-dimensional materials with unique properties led to the discovery of MXenes in 2011. At a very early stage of MXene research theoretical and experimental studies on the use of $Ti_3C_2T_x$ in LIBs were carried out. Already in the first paper on $Ti_3C_2T_x$, computational calculations were run to predict the theoretical capacity of the material, indicating a capacity of 320 mAh g^{-1} for the lithium-ion intercalation into the space that used to be occupied by aluminium in the MAX phase via the reaction [31]:

$$Ti_3C_2 + 2\,Li^+ + 2\,e^- = Ti_3C_2Li_2 \tag{4.1}$$

This specific capacity is comparable with the one for graphite and therefore potentially interesting. Tang et al. have reported similar results based on the density functional theory [113] for lithium adsorption on a bare Ti_3C_2 sheet (320 mAh g^{-1}) as well as calculated the specific capacity for functionalised $Ti_3C_2T_x$ sheets. In the case of lithium adsorption on the terminated $Ti_3C_2T_x$ MXene sheet, the capacity was 130 mAh g^{-1} for the F-terminated $Ti_3C_2F_2$ and 67 mAh g^{-1} for the OH-terminated $Ti_3C_2(OH)_2$. The standard potentials for the lithiation reaction of the Ti_3C_2, $Ti_3C_2F_2$ and $Ti_3C_2(OH)_2$ were estimated to be 0.62 V, 0.56 V and 0.14 V vs. Li^+/Li, respectively. These values are comparable with the intercalation potential of $\sim$0.2 V vs. Li^+/Li for graphite, and make it reasonable to assume that, similarly to graphite, the carbon in $Ti_3C_2T_x$ should undergo reduction at these potentials. Since it was shown that synthesised $Ti_3C_2T_x$ flakes are always terminated [114, 115], the practically observed capacities should be lower than 320 mAh g^{-1} and stem from the reaction

$$Ti_3C_2T_x + 2\,Li^+ + 2\,e^- = Ti_3C_2T_xLi_2 \tag{4.2}$$
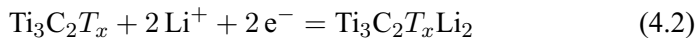
The first practical evaluation of the $Ti_3C_2T_x$ specific capacity, where T was a mixture of -OH, -F and =O terminations, showed, however, an even higher reversible capacity on cycling, 410 mAh g^{-1} at 1C for over 100 cycles [39]. In an attempt to explain this discrepancy between the theoretically and practically obtained values, new computational calculations were published, where the higher experimental capacities were interpreted by assuming that already lithiated $Ti_3C_2O_2Li_2$ adsorbed an extra layer of lithium [116]. The reasoning behind this explanation, however, seems implausible, as will be shown below.

Nevertheless, this explanation arose due to the fact that the experimental XAS results showed only a minor change in the oxidation state change of titanium in $Ti_3C_2T_x$ upon cycling which was not able to explain the observed capacity on the first cycle.

The redox reaction, *Equation 4.2*, raised questions regarding the origin of the capacity seen for $Ti_3C_2T_x$ electrodes cycling in LIBs, as it was not specified which element underwent the reduction, titanium and/or carbon. Other issues such as the significantly different capacities reported for $Ti_3C_2T_x$ electrodes [76, 77] in LIBs, and the origin of the large irreversible capacity, often seen on the first cycles [39], were neither properly explained. Moreover, it was also suggested that $Ti_3C_2T_x$ electrodes can yield high capacities in Na-ion batteries (SIBs), with a predicted capacity of 300 mAh g^{-1} for $Ti_3C_2O_2$ [117] and practically achieved capacity of 100 mAh g^{-1} at 20 mA g^{-1} [118] or 50 mA g^{-1} [119] and even 160 mAh g^{-1} at 20 mA g^{-1} if a water-free $Ti_3C_2T_x$ synthesis is used [71]. Lastly, an increase of the $Ti_3C_2T_x$ electrodes capacity upon cycling in LIBs ("activation") was reported in the literature [75, 120], and the origin of this phenomenon remains a subject of debate.

4.1.1 Origin of the capacity

The suggested redox reaction for the $Ti_3C_2T_x$ electrode, *Equation 4.2*, was further discussed in **Paper I**. It was investigated if this reaction really takes place upon the cycling of $Ti_3C_2T_x$ electrodes in LIBs and which element, titanium or carbon, undergoes the reduction on lithiation.

To be able to specify the redox reaction, it is important to first identify the oxidation states of both titanium and carbon in the $Ti_3C_2T_x$ flake.

An analysis of the chemical reactions taking place during the synthesis of $Ti_3C_2T_x$, for example, the reaction
$Ti_3C_2 + 2\,H_2O = Ti_3C_2(OH)_2 + H_2$ [31], shows that this reaction can be divided into the following reduction and oxidation reactions:
$2\,H_2O + 2\,e^- = 2\,OH^- + H_2$ (reduction),
$Ti_3C_2 + 2\,OH^- = Ti_3C_2(OH)_2 + 2\,e^-$ (oxidation).
The relevant standard reduction potentials for titanium and carbon are

$$Ti^{2+} + 2\,e^- = Ti, \; E^0 = 1.4\,V \text{ vs. } Li^+/Li \qquad (4.3)$$

$$CO_2 + 4\,H^+ + 4\,e^- = C + 2\,H_2O, \; E^0 = 3.2\,V \text{ vs. } Li^+/Li \qquad (4.4)$$

respectively. As it can be seen from the standard reduction potentials, titanium is more easily oxidised than carbon, therefore the above-mentioned oxidation reaction should mainly involve the titanium and then predominantly the titanium that is present on the surfaces of the $Ti_3C_2T_x$ flakes. In *Figure 4.1C*, two different titanium species in a $Ti_3C_2T_x$ flake are shown: Ti2 in the surface T_x-Ti-C layer and Ti1 in the core Ti-C layer of the flake.

According to the above-mentioned $Ti_3C_2OH_2$ oxidation reaction during the synthesis, two Ti2 should be oxidised to Ti(I) each, while Ti1 should have an oxidation state of 0. Here it should be noted that carbon is a poor oxidising agent and hence unable to oxidise titanium. Moreover the Ti-C peak attributed to the core Ti-C layer of the $Ti_3C_2T_x$ flake remained pronounced and unchanged for the electrodes analysed post hoc with XPS, that is why it was concluded that Ti1 species were electroinactive. The average titanium oxidation state in the $Ti_3C_2T_x$ flake should then be quite low, +0.67. Reversible cycling of $0.67\,e^-$ per formula unit would result in a capacity of $\sim 84\,\text{mAh\,g}^{-1}$,
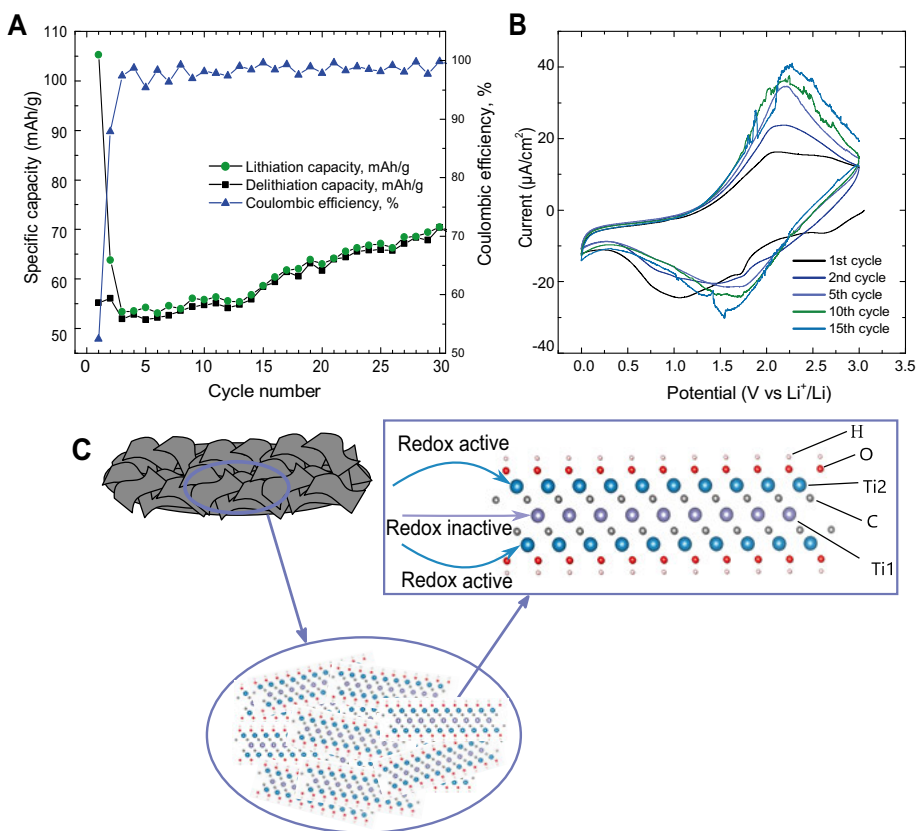

Figure 4.1. **A**: The lithiation (reduction) and delithiation (oxidation) capacities as well as the coulombic efficiency as a function of the cycle number for a freestanding $Ti_3C_2T_x$ electrode for constant current cycling with a current density of 10 mA g^{-1} from 0.01 to 3 V vs. Li^+/Li. **B**: cyclic voltammograms recorded for an analogous electrode at a scan rate of $0.1\,\text{mV\,s}^{-1}$. **C**: Schematic illustrations depicting a freestanding $Ti_3C_2(OH)_2$ electrode (top left), a magnification of the $Ti_3C_2T_x$ flakes within the bulk of the electrode (bottom) as well as the structure of an individual $i_3C_2T_x$ MXene flake (top right). Ti1 denotes the titanium in the Ti-C layer, whereas Ti2 denotes the titanium in a T_x-Ti-C layer.

according to *Equation 1.1* and using the averaged molar mass of a $Ti_3C_2T_x$ flake, 215 g mol^{-1}. If the flakes are exposed to air or water, the oxidation of titanium to TiO_2 should spontaneously occur [121, 122]. The oxidation of titanium metal to TiO_2, where titanium has the oxidation state of (IV), involves the sequential loss of four electrons, meaning that the oxidation should involve Ti(I), Ti(II), and Ti(III) oxidation states as intermediate species. This means that the titanium in the Ti2 s can be present in the oxidation states of Ti(I, II, III, IV) depending on the experimental conditions. These titanium species should be able to take part in the redox reactions and contribute to the lithiation and delithiation capacities.

Which redox reactions are possible for Ti2(I, II, III, IV) species? As was mentioned above, the standard potential for the Ti(II)/Ti(0) redox reaction is 1.4 V vs. Li$^+$/Li, meaning that at potentials below this value, titanium should exist in the elemental state, and the lithiation (reduction) of Ti(I, II, III, IV) species should take place at potentials above 1.4 V vs. Li$^+$/Li. If TiO_2 is present on the surface, its lithiation should take place at a potential of about 1.8 V vs. Li$^+$/Li, according to *Equation 1.3* (typically with the reduction peak at $\sim$1.6 V and the oxidation peak at $\sim$2 V vs. Li$^+$/Li), while a conversion reaction

$$TiO_2 + 4\,Li^+ + 4\,e^- = Ti + 2\,Li_2O \qquad (4.5)$$
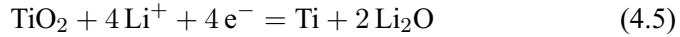
could be expected at about 0.6 V vs. Li$^+$/Li. Carbon can theoretically be reduced to Li_2C_2, and such a reaction would look like

$$2\,C + 2\,Li^+ + 2\,e^- = Li_2C_2 \qquad (4.6)$$
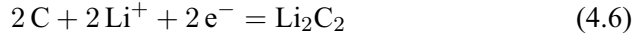
and appear in the vicinity of 0.3 V vs. Li$^+$/Li.

Which of the redox reactions, corresponding to *Equation 4.3*, *Equation 4.5*, or *Equation 4.6*, are taking place upon $Ti_3C_2T_x$ electrode cycling in a LIB and hence contribute to the capacity? The very first observation when looking at the CC cycling data was that the capacity of a freestanding $Ti_3C_2T_x$ electrode was $\sim$67 mAh g^{-1} when cycled at 10 mA g^{-1} for 30 cycles, *Figure 4.1A*, which is considerably lower than the predicted 320 mAh g^{-1} and previously observed 410 mAh g^{-1}. Moreover, this performance is considered to be poor in comparison with the commercially used graphite with the specific capacity of 372 mAh g^{-1}. According to the cyclic voltammograms, the observed capacity for $Ti_3C_2T_x$ electrode originated from the broad lithiation (reduction) peak at 1.6 V and the broad delithiation (oxidation) peak at about 2.2 V vs. Li$^+$/Li, *Figure 4.1B*. These redox reactions can therefore be attributed to the Ti2(I), Ti2(II), Ti2(III), and Ti2(IV) species in the T_x-Ti-C surface layer of the $Ti_3C_2T_x$ flakes in the $Ti_3C_2T_x$ electrode. No redox peaks were observed at $\sim$0.3 V Li$^+$/Li, and, similarly, neither reduction nor oxidation took place at $\sim$0.6 V Li$^+$/Li, which indicated that no reduction of carbon nor a TiO_2 conversion reaction took place on the cycling.

Do the redox reactions of Ti2(I-IV) species involve the majority of the flakes within the bulk of the $Ti_3C_2T_x$ electrode? The ex-situ Ti K-edge XAS in the

transmission data for the cycled $Ti_3C_2T_x$ electrodes revealed no considerable change in the oxidation state of titanium in the bulk of the electrode on the first cycle (no considerable shift of the Ti K-edge on cycling), *Figure 4.2A*.
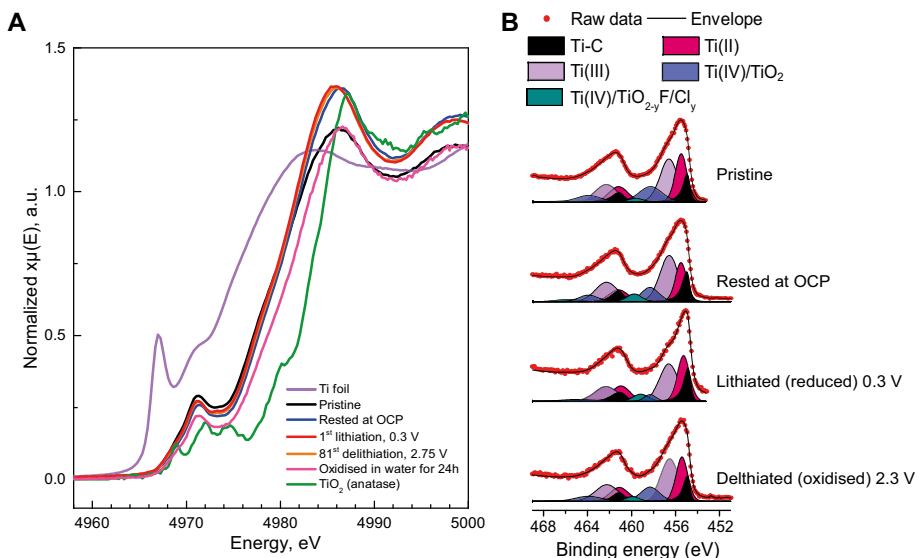

Figure 4.2. **A**: Ti K-edge XAS spectra obtained for a pristine $Ti_3C_2T_x$ electrode, an electrode rested at OCP (blue), an electrode lithiated to 0.3 V vs. Li^+/Li on the first cycle (red), an electrode delithiated to 2.75 V vs. Li^+/Li on the 81st cycle (orange) and an electrode exposed to water and air for 24 hours at room temperature (pink). The spectra for a titanium foil (purple) and TiO_2 anatase (green) have been included for comparison. **B**: XPS Ti2p spectra for a pristine $Ti_3C_2T_x$ electrode, an electrode rested at OCP, an electrode lithiated (reduced) to 0.3 V vs. Li^+/Li on the first cycle as well as an electrode delithiated (oxidised) to 2.3 V vs. Li^+/Li on the first cycle, respectively.

The XPS data, revealed a slight change in the distribution of titanium oxidation states (II, III, IV) on the surface of the $Ti_3C_2T_x$ electrode on the first lithiation (relative decrease) and delithiation (relative increase), *Figure 4.2B*. It should be mentioned that the Ti(I) oxidation state is considered to be unstable and is difficult to trace with XPS, moreover, the peak at 458.3 eV was assigned to TiO_2, but generally, it can also represent $TiO(OH)_2$, $Ti(OH)_4$ or similar Ti(IV) species, while the peak at 459.8 eV was assigned to $TiO_{2-x}F_x$, but it can also represent $TiO_{2-y}Cl_y$, $TiCl_4$, TiF_4 or similar halogenated Ti(IV) species. Therefore, it was concluded that only the surface of the $Ti_3C_2T_x$ electrode was redox active while there were difficulties associated with the oxidation/reduction of each individual flake within the bulk of the $Ti_3C_2T_x$ electrode due to the restacking of the flakes. This is, however, bad news for $Ti_3C_2T_x$ as a battery material, since electroinactive flakes are nothing else but a dead weight in an electrode and a battery.

Analogous redox reactions are expected to take place upon $Ti_3C_2T_x$ electrode cycling in SIBs, with a difference that the redox reactions should be found at lower potentials and that the gravimetric capacities are expected to be lower in comparison with the $Ti_3C_2T_x$ electrode in LIBs. The standard reduction potential for the Ti(0)/Ti(II) redox couple, *Equation 4.3*, should translate to 1.1 V vs. Na^+/Na. As it was shown in **Paper II**, similar to the $Ti_3C_2T_x$/Li cell, the cyclic voltammograms for the $Ti_3C_2T_x$/Na cell featured broad reduction and oxidation peaks, but at 1.3 and 2 V vs. Na^+/Na, respectively, see *Figure 4.3B*.
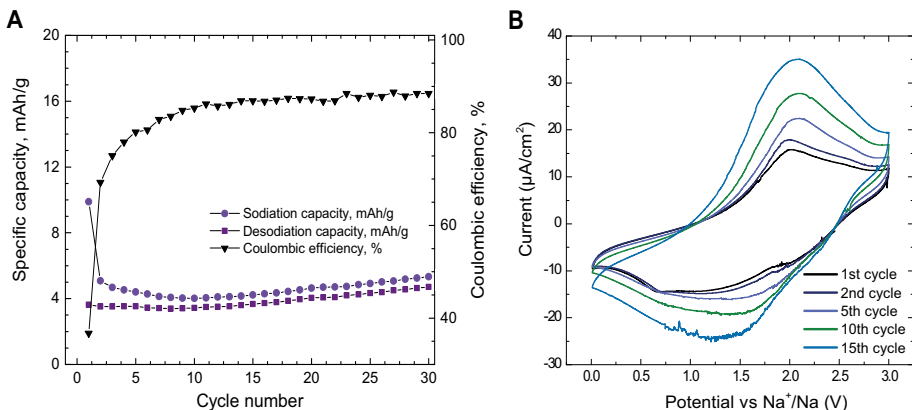

Figure 4.3. **A**: The sodiation (reduction) and desodiation (oxidation) capacities as well as the coulombic efficiency as a function of the cycle number for a freestanding $Ti_3C_2T_x$ electrode for constant current cycling with a current density of 10 mA g^{-1} from 0.01 to 3 V vs. Na^+/Na. **B**: Cyclic voltammograms recorded for an analogous electrode at a scan rate of 0.1 mV s^{-1}.

Similarly to the lithium-case, these peaks were ascribed to the reduction and oxidation of Ti(I), Ti(II), Ti(III), and Ti(IV) titanium species in the T_x-Ti-C surface layer of the $Ti_3C_2T_x$ flakes. As expected, the CC cycling for the $Ti_3C_2T_x$ electrode in the SIB yielded lower capacities in comparison to the cycling in the LIB, only ~5 mAh g^{-1} after 30 cycles, *Figure 4.3A*.

Therefore, the energy storage mechanism in $Ti_3C_2T_x$ electrode was predominantly Faradic, i.e., based on redox reactions.

4.1.2 Capacity variation and irreversible capacity

As was mentioned in the introduction, the capacities reported for chemically similar $Ti_3C_2T_x$ electrodes varied significantly in the literature. In addition, irreversible capacities on the initial cycles were often observed for $Ti_3C_2T_x$ electrodes but rarely properly addressed. Hence, it was crucial to find a suitable explanation for both of these observations and a part of **Paper I** was dedicated to achieving this.

As shown previously, $Ti_3C_2T_x$ undergoes oxidation to TiO_2 when exposed to air or water [75, 123]:

$$2\,Ti_3C_2OH_2 + 5\,O_2 = 6\,TiO_2 + 2\,H_2O + 4\,C \qquad (4.7)$$
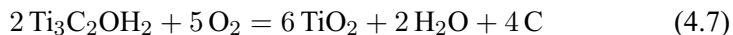
The reaction is spontaneous and the oxidation of $Ti_3C_2T_x$ is usually prevented by minimising its exposure to air and oxygen. Titanium dioxide is the final product of the oxidation and the existence of the intermediate species with oxidation states Ti(I), Ti(II), and Ti(III) are also expected, as was already pointed out above. Depending on the conditions employed during the synthesis and post-synthesis treatment (e.g., if the synthesis and/or delamination of $Ti_3C_2T_x$ powder was done in water, if delamination was done under argon or in air, if electrodes were dried after manufacture or not, etc.) the average oxidation state of titanium in $Ti_3C_2T_x$ and subsequently the capacity of $Ti_3C_2T_x$ electrodes should be higher or lower. Since the Ti2(I-IV) species on the surface of $Ti_3C_2T_x$ electrode were found to be redox active, their concentration will directly affect the capacity of $Ti_3C_2T_x$ electrode in lithium- and sodium-ion cells.

To demonstrate the $Ti_3C_2T_x$ electrochemical performance dependence on the degree of surface oxidation in a LIB, a suspension oxidation experiment was performed. A vial of freshly prepared $Ti_3C_2T_x$ suspension in water was exposed to air for 28 days. On the 7th, 14th and 28th day of the experiment, 5 mL of the suspension was taken from the vial with a syringe and vacuum filtrated to obtain a freestanding film electrode. These electrodes were then subjected to CV cycling and XPS, *Figure 4.4*.

All of the cycling voltammograms when cycled between 0.8 and 3.0 V vs. Li^+/Li in *Figure 4.4A* featured a lithiation peak at about 1.7 V and a delithiation peak at about 2.2 V vs. Li^+/Li, similar to what was seen for a $Ti_3C_2T_x$ electrode cycled to 0.01 V vs. Li^+/Li. The lower cut-off potential of 0.8 instead of 0.01 V vs. Li^+/Li was chosen to avoid a possible TiO_2 conversion reaction, *Equation 4.5*. The reduction and oxidation peak currents increased with the number of days the $Ti_3C_2T_x$ suspension was left exposed to air, from about 20 μA/cm^2 before the oxidation to about 80 μA/cm^2 on the 28th day of oxidation, respectively. This indicates that the oxidation of $Ti_3C_2T_x$ flakes in air and water improved the capacity observed for the electrodes prepared from these flakes.

This capacity increase is better seen in the lithiation and delithiation capacities extracted from the CV, *Figure 4.4B*. For the pristine (0 days) electrode and the electrode prepared from the $Ti_3C_2T_x$ exposed to water and air for seven days, the capacities were about 21 and 50 mAh g^{-1} after 25 cycles, respectively. The lithiation capacities for the 14-day and 28-day electrodes were higher and equalled 68 mAhg^{-1} and 74 mAh g^{-1}, respectively. When comparing the obtained capacities with that of about 168 mAh g^{-1} for the lith-

iation of anatase, TiO_2 to $Li_{0.5}TiO_2$ [18, 124], it is clear that only a fraction of the MXene flakes underwent titanium oxidation to higher oxidation states.
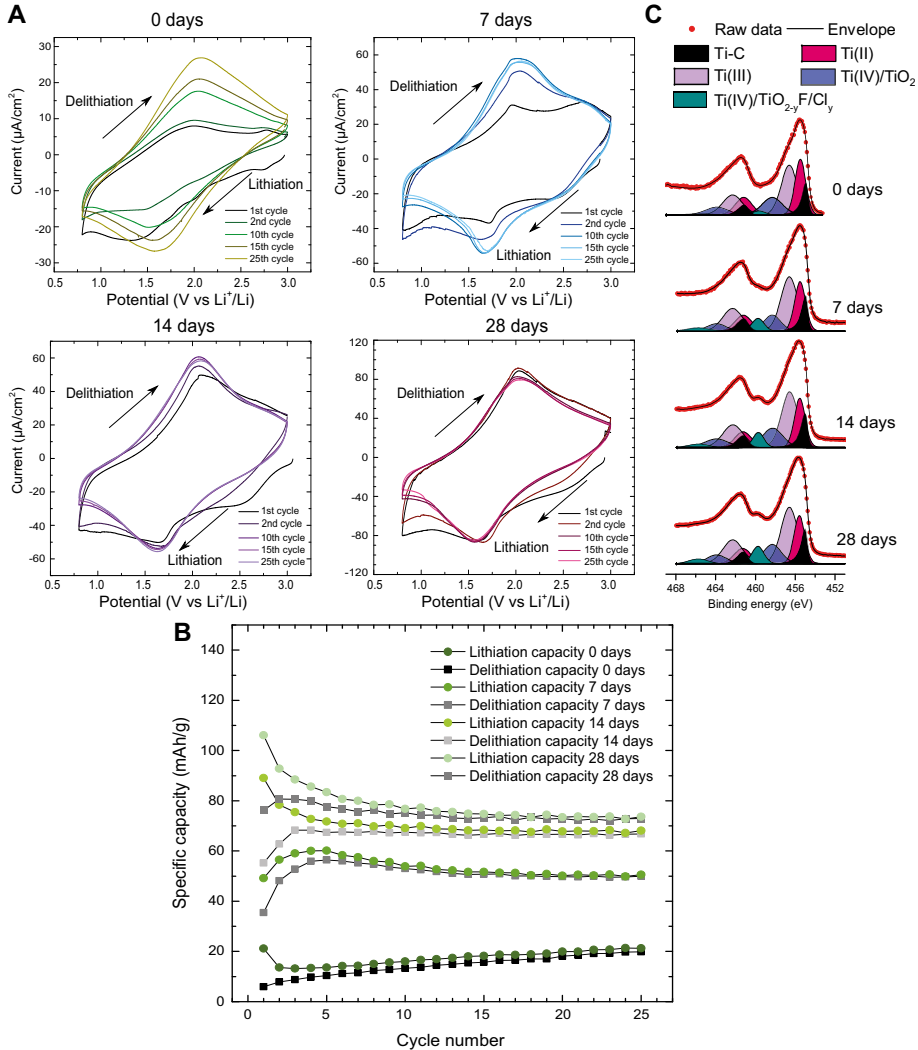

Figure 4.4. **A**: Cyclic voltammograms recorded at a scan rate of 0.1 mV s^{-1} from 0.8 to 3 V vs. Li$^+$/Li for a pristine freestanding $Ti_3C_2T_x$ film electrode (0 days) and electrodes made from a suspension of $Ti_3C_2T_x$ in deionised water exposed to air in an open vial for 7, 14 and 28 days, respectively. **B**: Lithiation and delithiation capacities extracted from the cyclic voltammograms as a function of the cycle number for the above-mentioned electrodes. **C**: XPS Ti2p spectra for analogous electrodes.

The XPS data for analogous electrodes support this hypothesis and reveal a relative increase in the TiO_2 peak at 458.3 eV and $TiO_{2-x}F_x$ peak at 459.8 eV on the surface of $Ti_3C_2T_x$ electrodes during the oxidation experiment (*Figure 4.4C*).

It is reasonable to conclude that the $Ti_3C_2T_x$ flakes were partially converted to TiO_2 (and $TiO_{2-x}F_x$) within 28 days of exposure to air and water. Such oxidation significantly increased the lithiation and delithiation capacities of the $Ti_3C_2T_x$ electrodes. The average oxidation degree of a pristine $Ti_3C_2T_x$ electrode was relatively low, based on the XPS data in *Figure 4.4C* the relative concentration of Ti(IV) and Ti(III) species for the pristine electrode was 0.59 and for the electrode after 28 days of oxidation the corresponding value was 0.65. Therefore the pristine $Ti_3C_2T_x$ electrode showed a quite low capacity upon cycling.

A considerable irreversible capacity loss was observed for $Ti_3C_2T_x$ electrodes on the initial cycles in lithium- and sodium-cells, *Figure 4.1* and *Figure 4.3*, respectively. In the literature this phenomenon is quite often ascribed to solid electrolyte interphase (SEI) formation [75, 117] or, more recently, even to $Ti_3C_2T_x$ irreversible structural changes due to solvent co-intercalation upon the lithiation [120]. In contrast, in **Paper I** it was shown that a capacity loss due to SEI formation was indeed present in the first lithiation/delithiation cycle(s), however, it could explain only about 30% of the observed capacity loss on the first three cycles. The reduction of water and the inability to fully regenerate the oxidised titanium and carbon species on the delithiation step, could explain the remaining 70%.

From previous reports it is known that water could be adsorbed on the surfaces and become confined between MXene flakes [73, 116, 125]. For titanium dioxide electrodes it is known that reduction of adsorbed water can give rise to large irreversible capacities: H_2O/OH species adsorbed on TiO_2 surfaces can become reduced to yield H_2 and Li_2O [17]. Since $Ti_3C_2T_x$ flakes can be -OH and =O terminated, it is reasonable to assume that a similar phenomenon can be observed for $Ti_3C_2T_x$ electrodes.

To test the hypothesis that the reduction of water gave rise to a major contribution to the observed irreversible capacity, an experiment comparing CV and CC cycling of a $Ti_3C_2T_x$ electrode dried at an elevated temperature (i.e., 300 °C) and of a non-dried $Ti_3C_2T_x$ electrode was performed.

A comparison of the cyclic voltammograms in *Figures 4.5B* and *C* clearly shows a larger irreversible capacity on the first cycle for the non-dried electrode. It can also be seen that only a relatively small part of the irreversible capacity stemmed from the SEI formation, i.e., reduction below 1 V vs. Li^+/Li. The latter suggests that the reduction of the water adsorbed on the surface of $Ti_3C_2T_x$ electrode and confined in between the $Ti_3C_2T_x$ flakes was the main reason of the observed irreversible capacity.

The data extracted from the CC cycling are in good agreement with the cyclic voltammograms. *Figure 4.5A* shows a considerable decrease in the irreversible lithiation capacity for the $Ti_3C_2T_x$ electrode dried at 300 °C on the first cycle, 16 mAh g^{-1} compared to 50 mAh g^{-1} for an electrode dried at 120 °C, *Figure 4.1A*.
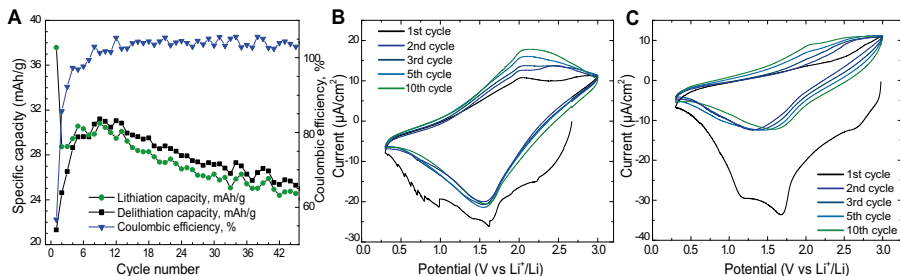
Figure 4.5. **A**: Lithiation and delithiation capacities and coulombic efficiency as a function of the cycle number for the CC cycling at 10 mA g^{-1} for a freestanding Ti$_3$C$_2$T$_x$ electrode dried for 16 hours at 300 °C under vacuum. Cyclic voltammograms recorded at a scan rate of 0.1 mV s^{-1} from 0.3 to 3 V vs. Li$^+$/Li for **B**: a freestanding Ti$_3$C$_2$T$_x$ electrode dried for 16 hours at 300 °C under vacuum and **C**: a non-dried freestanding Ti$_3$C$_2$T$_x$ electrode.

It was therefore concluded that the major contribution to the irreversible capacity observed for the Ti$_3$C$_2$T$_x$ electrodes in LIBs should come from the reaction:

$$H_2O + 2\,Li^+ + 2\,e^- = H_2 + Li_2O,\ E^0 = 1.6\,V\ vs.\ Li^+/Li \qquad (4.8)$$
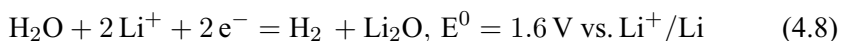
For the pristine Ti$_3$C$_2$T$_x$ electrode used in *Figure 4.1A*, with the mass of 1.31 mg, 70% of the irreversible capacity observed on the first three cycles can be explained by the reduction of 19 μg of water. That corresponds to a water concentration as low as 1.4 wt.% in the electrode.

For the Ti$_3$C$_2$T$_x$/Na cell, the analogous reaction should be

$$H_2O + 2\,Na^+ + 2\,e^- = H_2 + Na_2O,\ E^0 = 0.7\,V\ vs.\ Na^+/Na \qquad (4.9)$$
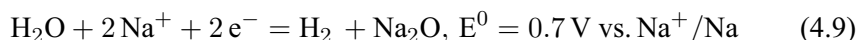
However, it is difficult to distinguish the water reduction peak at about 0.7 V vs. Na$^+$/Na on the cyclic voltammograms since it overlapped with the cascade of the Ti2 species reduction reactions, *Figure 4.3B*. Moreover, the capacity loss observed on the first cycle of the CC cycling was only 5 mAh g^{-1} for the Ti$_3$C$_2$T$_x$ electrode in the SIB, which is about ten times smaller in comparison with the 50 mAh g^{-1} seen in the LIB, in *Figure 4.1B*. Possibly larger sodium ions cannot diffuse as easily as smaller lithium ions within the Ti$_3$C$_2$T$_x$ electrode structure and react with the water trapped between the Ti$_3$C$_2$T$_x$ flakes. Alternatively, it was more difficult to fully regenerate the oxidised titanium species on the desodiation step, compared to the delithiation step.

4.1.3 Capacity activation on cycling

The understanding of the redox reactions taking place on Ti$_3$C$_2$T$_x$ electrode cycling in LIBs and SIBs was further developed and applied to explain the ca-
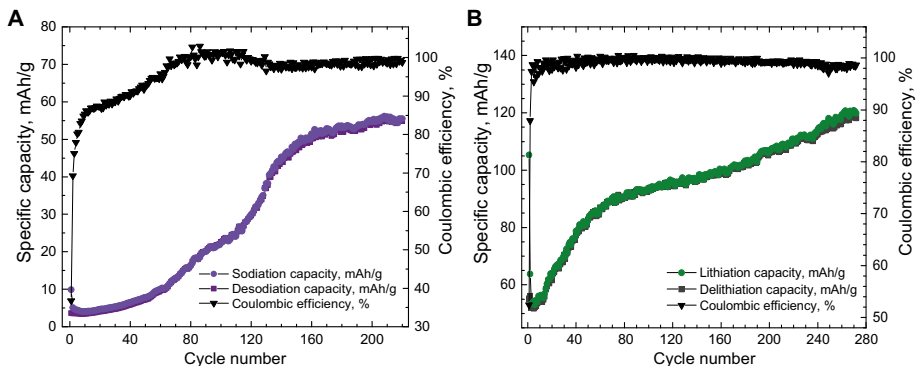
Figure 4.6. **A**: The sodiation (reduction) and desodiation (oxidation) capacities as well as the coulombic efficiency as a function of the cycle number for a freestanding $Ti_3C_2T_x$ electrode extracted from constant current cycling with a current density of 10 mA g^{-1} between 0.01 and 3 V vs. Na$^+$/Na (the long-term cycling of the cell presented in *Figure 4.1***A**). **B**: The lithiation (reduction) and delithiation (oxidation) capacities as well as the coulombic efficiency as a function of the cycle number for a freestanding $Ti_3C_2T_x$ electrode for constant current cycling with a current density of 10 mA g^{-1} between 0.01 and 3 V vs. Li$^+$/Li, (the long-term cycling of the cell presented in *Figure 4.3***A**).

pacity activation phenomenon seen during long-term cycling, i.e., when cycling for more than 200 cycles, in **Paper II**.

It is logical to assume that the observed capacity increase during cycling was either caused by the oxidation of the redox active species to higher oxidation states and/or the increase of the number of active species due to the electrode structure opening up on cycling, i.e., that species that were not initially in the contact with electrolyte became accessible for the electrolyte after several cycles and, hence, started to be redox active.

The data extracted from the CC cycling between 0.01 and 3 V vs. Na$^+$/Na for over 200 cycles in a SIB cell, clearly show that the sodiation and desodiation capacities of the $Ti_3C_2T_x$ electrode increased with the cycle number from 4 mAh g^{-1} on the first cycle to 55 mAh g^{-1} on the 220th cycle, *Figure 4.6B*. Moreover, a similar behaviour was found for a $Ti_3C_2T_x$/Li cell, where the delithiation capacity increased from 55 mAh g^{-1} on the first cycle to 110 mAh g^{-1} on the 220th cycle, *Figure 4.6B*.

Since the capacity increase was relatively similar in both cases, of the order of 50 mAh g^{-1} in both a LIB and a SIB cell, it was suggested that the activation effects had the same origin. Owing to the fact that the electrodes were manufactured in the same way, it was anticipated that the amount of water trapped between the $Ti_3C_2T_x$ sheets was the same, and this water enabled a progressive titanium species oxidation in $Ti_3C_2T_x$ electrodes to higher oxidation states.

Alternative explanations for the activation were also suggested, for instance, underpotential sodium deposition on the surface of the $Ti_3C_2T_x$ electrode and

its chemical reaction with sodium. Nevertheless, sodium deposition experiments resulted in stabilisation of the capacity at low levels (5 mAh g^{-1} from the first and up to 200th cycle). An increase of the lower cut-off potential on CC cycling to 0.8 or 1.1 V vs. Na$^+$/Na still resulted in capacity activation of the Ti$_3$C$_2$T$_x$ electrodes, although less pronounced (the capacity increased from 3 mAh g^{-1} on the first cycle to 12 mAh g^{-1} on the 220th cycle in both cases). It was therefore excluded that sodium deposition was causing the activation of the material.

Ex situ XAS results for Ti$_3$C$_2$T$_x$ electrodes cycled vs. sodium metal confirmed that oxidation of titanium species to higher oxidation states took place in the Ti$_3$C$_2$T$_x$ electrodes on long-term cycling, *Figure 4.7*.
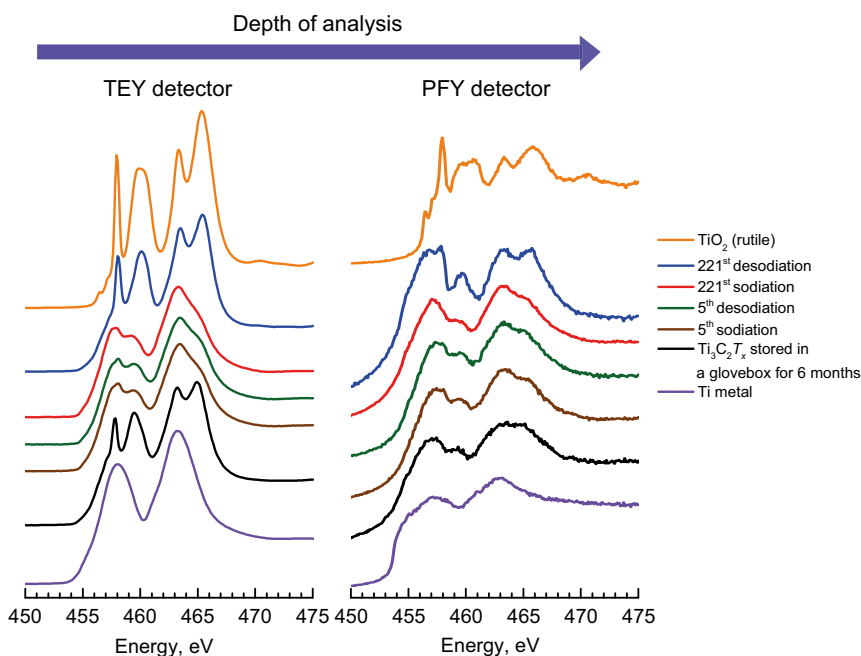

Figure 4.7. **A**: Ti L-edge XAS spectra collected with the TEY and PFY detectors (left and right, respectively) for Ti$_3$C$_2$T$_x$ electrodes on the 5th and 221st sodiation and desodiation steps, as well as for a Ti$_3$C$_2$T$_x$ electrode stored in a glovebox for 6 months, Ti metal and TiO$_2$ (rutile) crystal.

On the 221st sodiation step, the surface of the Ti$_3$C$_2$T$_x$ electrode looked similar to the surface of TiO$_2$ rutile crystal, based on the similarity of the spectra collected with the TEY detector (the depth of analysis with the TEY detector was up to $\sim$5 nm), see *Figure 4.7*, left. The bulk of the Ti$_3$C$_2$T$_x$ electrode on the 221st sodiation step looked less oxidised, based on the fact that its spectrum collected with the PFY detector (the depth of analysis with the PFY detector is up to $\sim$100 nm) showed some features of the rutile spectrum, i.e., a peak at 458 eV, but mostly resembled the spectrum for a non-cycled Ti$_3$C$_2$T$_x$

electrode stored in a glovebox, *Figure 4.7*, right. Therefore, it was concluded that titanium in the $Ti_3C_2T_x$ electrode underwent oxidation to higher oxidation states, which caused the capacity to increase upon long-term cycling.

From comparing the spectra recorded for the $Ti_3C_2T_x$ electrode on the 5th sodiation and desodiation step with the PFY detector, one can conclude that the bulk of $Ti_3C_2T_x$ electrode remained electroinactive, while almost identical Ti L-edge spectra were collected with the TEY detector. These observations agree with the low capacity seen on the fifth cycle, about 5 mAh g^{-1}, *Figure 4.6*A.

A comparison of the cyclic voltammograms obtained for a $Ti_3C_2T_x$ electrode on the 200th cycle, *Figure 4.8D*, with the cyclic voltammograms recorded for amorphous and crystalline anatase TiO_2 nanotube electrodes as well as for a crystalline anatase TiO_2 nanoparticle composite electrode, *Figure 4.8A*, C and B, respectively, shows that the $Ti_3C_2T_x$ redox peaks cannot be ascribed to sodiation and desodiation of TiO_2.
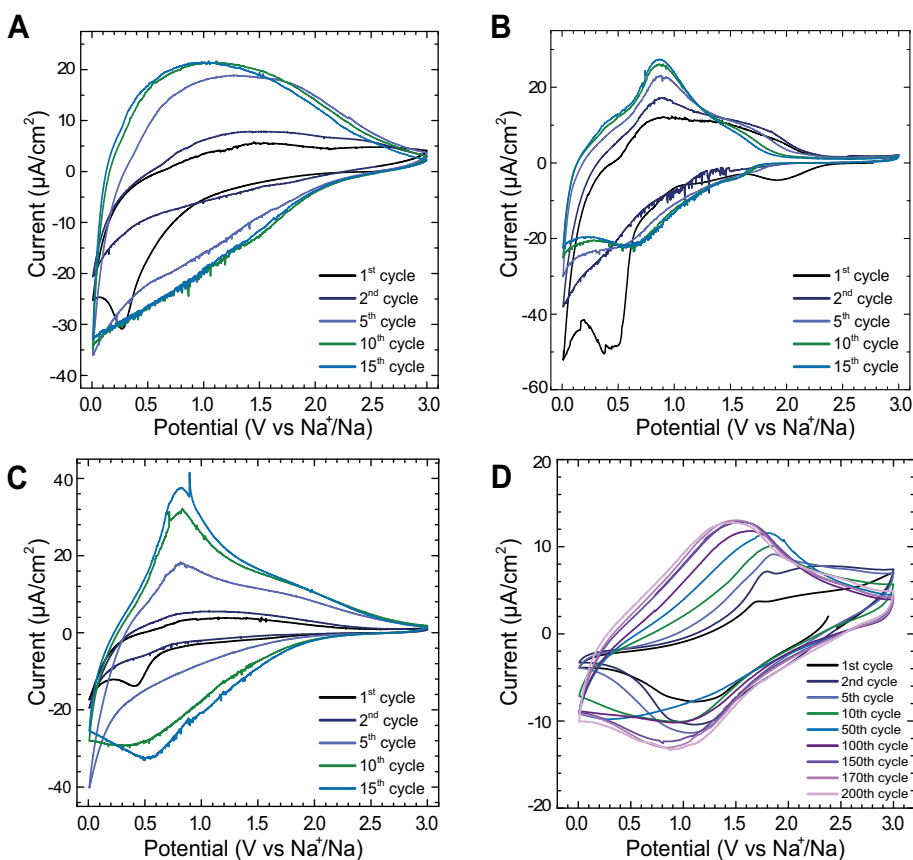

Figure 4.8. Cyclic voltammograms recorded at a scan rate of 0.1 mV s^{-1} from 0.01 to 3 V vs. Na^+/Na for **A**: an amorphous TiO_2 nanotube electrode, **B**: a crystalline anatase TiO_2 nanoparticle composite electrode, **C**: a crystalline anatase TiO_2 nanotube electrode, and for **D**: a $Ti_3C_2T_x$ electrode.

Indeed, crystalline anatase TiO_2 electrodes showed relatively sharp reduction and oxidation peaks at about 0.6 and 0.8 V vs. Na^+/Na, while similar but relatively broader peaks were seen for amorphous TiO_2 nanotube electrodes. In contrast, the $Ti_3C_2T_x$ electrode showed broad reduction and peaks at about 1.3 and 1.7 V on the initial cycles which were shifted to about 1.0 and 1.4 V vs. Na^+/Na on the 200th cycle. Therefore it is not likely that the $Ti_3C_2T_x$ electrode was oxidised to titanium (IV) dioxide during the long-term cycling. Nevertheless, the formation of the TiO_2 on the surface of the $Ti_3C_2T_x$ electrode is not mandatory for capacity activation, as the formation of any redox-active Ti2 species would yield an increased capacity.

To obtain information on which oxidised titanium species were formed during the cycling, pristine and cycled $Ti_3C_2T_x$ electrodes were analysed with XPS, *Figure 4.9*.

The deconvolution of Ti2p spectra for the electrodes cycled between 0.01 and 3 V vs. Na^+/Na and stopped on the first cycle as well as for the pristine and rested at OCP electrodes, showed an average titanium oxidation state of about +2.4, *Figure 4.9B*. As the cycling continued, the concentrations of the titanium surface species, i.e., C-Ti^{+2}-T_x containing Ti(II), C-Ti^{+3}-T_x containing Ti(III), TiO_2 and $TiO_{2-x}F_x$ (both containing Ti(IV)) started to change more drastically. On the 5th sodiation/desodiation cycle TiO_2 and $TiO_{2-x}F_x$ the relative peak area of the Ti(III) peak increased while the Ti(II) peak area decreased on the $Ti_3C_2T_x$ electrode desodiation in comparison with its sodiation. However, the relative peak area of the Ti(IV) peaks remained approximately the same as well as the oxidation state of titanium, about +2.7.

On the 225th desodiation step most of the titanium surface species ($\sim75\%$) reached the oxidation state of Ti(IV), while on the 225th sodiation step these species were partially reduced to Ti(III) and Ti(II), *Figure 4.9B*. The span in the titanium oxidation state on the 225th cycle was hence from +2.9 to +3.5. A similar behaviour was seen when a $Ti_3C_2T_x$ electrode was cycled vs. lithium metal, the XPS results for the $Ti_3C_2T_x$ electrode on the 283rd delithiation (oxidation) step showed a relatively high peak area for Ti(IV) surface species and an average titanium oxidation state of about +3.4.

When the lower cut-off potential was limited to 0.8 V vs. Na^+/Na on sodiation (reduction) the oxidation state span available for Ti was more limited: from +2.5 on sodiation (reduction) to +2.7 on desodiation (oxidation), *Figure 4.9B*. This observation agrees with the lower capacities obtained for the $Ti_3C_2T_x$ electrode when cycled between 0.8 and 3 V vs. Na^+/Na. Likewise this fact was reflected in the cyclic voltammograms, where the reduction at 0.8 V vs Na^+/Na was more incomplete in compared to when scanning down to 0.01 V vs. Na^+/Na, *Figure 4.10B*. The diffusion tail seen for the reduction peak observed at about 1 V when scanning to 0.01 V in *Figure 4.8D*, was cut off when scanning to 0.8 V vs. Na^+/Na.

Electrochemical impedance spectroscopy coupled with CV was then used to explore if an expansion of the $Ti_3C_2T_x$ electrode structure took place during

the cycling since an improved lithium-ion accessibility to active sites as a result of cycling was discussed previously [75, 120].
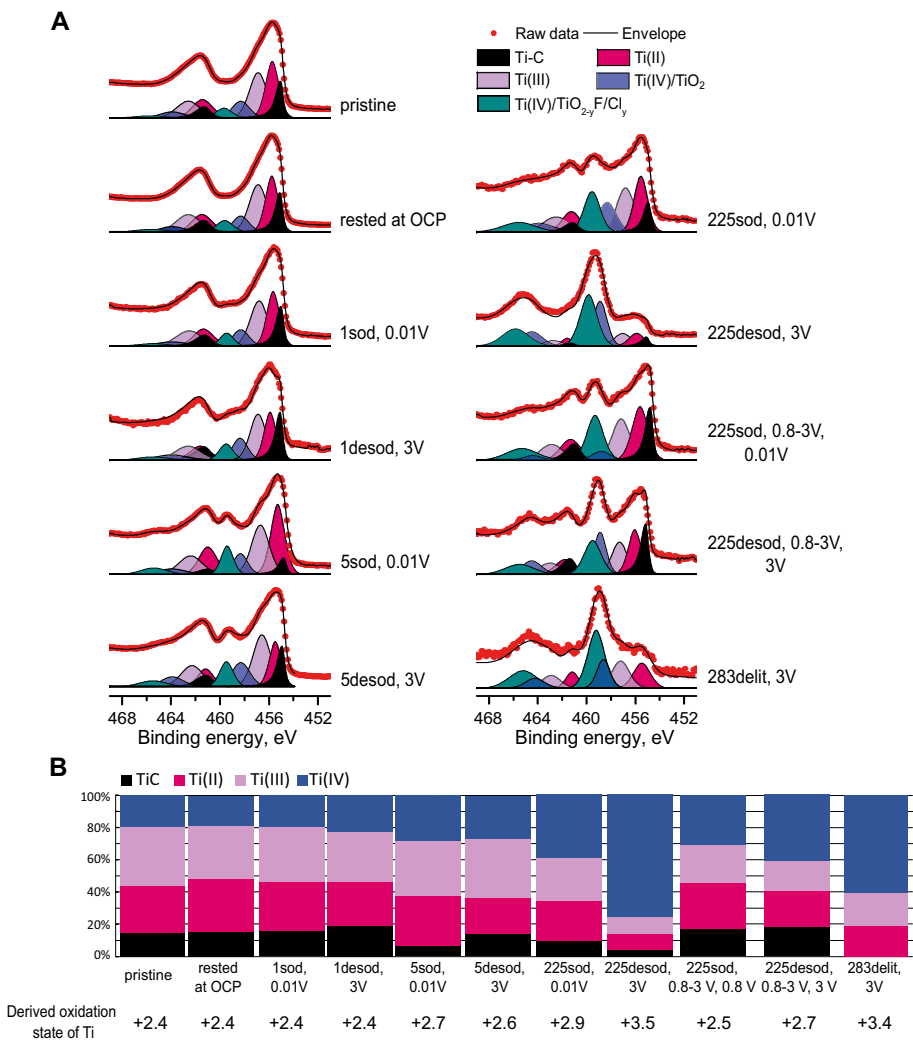
Figure 4.9. **A**: Ti2p region of pristine, rested at OCP and cycled for 1 and 5 cycles between 0.01 and 3 V vs. Na^+/Na $Ti_3C_2T_x$ electrodes (left) as well as $Ti_3C_2T_x$ electrodes cycled for 225 cycles between 0.01 and 3 V and 0.8 and 3 V vs. Na^+/Na potential windows (right) and stopped at indicated potentials. For comparison, data for the lithium half-cell cycled for 283 cycles between 0.01 and 3 V vs. Li^+/Li and stopped at 3 V are also provided (see the bottom right spectrum showing a similar trend for the LIB). **B**: a diagram showing the relative peak concentration of the Ti-C, Ti(II), Ti(III), and Ti(IV) species as well as the average oxidation state of titanium for each of the analysed electrodes derived from the XPS data.

44

Figure 4.10. **A**: Electrochemical impedance spectra for a $Ti_3C_2T_x$/Na cell recorded at the OCV (2.49 V vs. Na^+/Na) before cycling (black) and at 2.49 V vs. Na^+/Na after 150 (red) and 170 cycles (orange) when c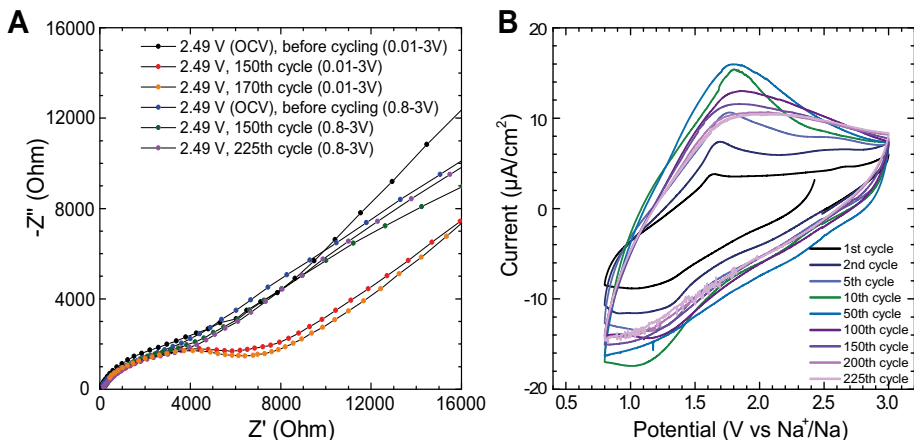ycled between 0.01 and 3 V vs. Na^+/Na. Impedance spectra were also collected for a $Ti_3C_2T_x$/cell cycled between 0.8 and 3 V: at the OCV (2.49 V vs. Na^+/Na) before cycling (blue) and at 2.49 V vs. Na^+/Na after 150 (green) and 225 cycles (purple). **B**: Cyclic voltammograms for a $Ti_3C_2T_x$ electrode collected at a scan rate of 0.1 mV s^{-1} between 0.8 and 3 V vs. Na^+/Na.

Electrochemical impedance spectra for all of the investigated cells showed semi-circles which implies the presence of a redox reaction rather than charge storage via a double-layer charging. The results for the $Ti_3C_2T_x$/Na cell rested at the open-circuit voltage, OCV, and cells cycled for 150 and 225 cycles between 0.8 and 3 V vs. Na^+/Na were quite similar to each other, *Figure 4.10A*. For the cell cycled between 0.01 and 3 V vs. Na^+/Na for 150 or 170 cycles the size of the semi-circle was increased in comparison with the one for the non-cycled cell. This observation indicates that in the case of cycling between 0.01 and 3 V vs. Na^+/Na, the redox reaction reached the diffusion control regime at relatively lower frequencies, meaning that in this case diffusion of sodium ions was faster in comparison with cycling between 0.8 and 3 V vs. Na^+/Na. It can be assumed as that the reduction during the long-term cycling to the 0.01 V cut-off potential required more sodium ions for charge neutralisation of the titanium species present in higher oxidation states. This in turn resulted in the structural expansion of the $Ti_3C_2T_x$ electrode which made sodium ions diffusion easier. However, since XAS results, *Figure 4.6B*, showed that the bulk of $Ti_3C_2T_x$ electrode mostly remained electroinactive and as the capacity of $Ti_3C_2T_x$ electrode remained comparatively low on the 220th cycle, 55 mAh g^{-1}, the degree of such expansion should still have been relatively low.

Therefore, it is concluded that there was both oxidation of the Ti2 redox-active species to higher oxidation states and that this caused the electrode structure to open up to some extent. This resulted in the involvement of more Ti2

redox-reactive species during the long-term cycling which can explain the observed capacity activation.

4.1.4 Effect of heat treatment on the capacity

Since it was shown in **Paper I** that it was difficult to eliminate water adsorbed on the surface of the $Ti_3C_2T_x$ electrode and trapped between the flakes even after drying at 300 °C for 16 hours, it was interesting to study if the use of higher temperatures could result in more complete water elimination. In situ XPS heating was therefore used in **Paper III** to track the $Ti_3C_2T_x$ electrodes' surface changes upon heating up to 775 °C. The capacity activation due to the oxidation of the titanium surface species discussed in **Paper II** was also further investigated in **Paper III**.

The results of the two different syntheses routes used for $Ti_3C_2T_x$ in **Paper III** were first studied and compared. The synthesis routes as well as the produced $Ti_3C_2T_x$ MXenes are referred to as $Ti_3C_2T_x$-LiF and $Ti_3C_2T_x$-HF in the text and the syntheses procedures are described in *Section 3.1*. It is evident from the outlined procedures that the syntheses were rather intricate, nevertheless, it was speculated that most of the F^- and Cl^- termination groups were introduced into the $Ti_3C_2T_x$ during the etching step, while the washings with water and the fact that both of the procedures were done in air inevitably introduced OH^- and O^{2-} terminations. The molar ratio between the parent MAX phase Ti_3AlC_2 and the etching reagents Ti_3AlC_2:HCl:LiF was 1:47:9 for the $Ti_3C_2T_x$-LiF film while Ti_3AlC_2:HCl:HF was 1:14:5 for the $Ti_3C_2T_x$-HF film. Since the concentration ratio Cl^-/F^- was almost twice as high in the first case, 5.2 compared to 2.8, one could expect that the $Ti_3C_2T_x$-LiF MXene would have a higher content of the Cl^- terminations compared to the $Ti_3C_2T_x$-HF sample. It was hypothesised that this fact could influence the electrochemical behaviour exhibited by the produced samples.

However, the XPS data in *Figure 4.11* show that both samples in their initial states, i.e., after the film preparation but prior to any heat treatment, exhibited very similar F^- (evaluated from the C-Ti-F peak areas) and Cl^- (evaluated from the survey spectra) termination contents.

A slight difference was seen for the oxygen termination contents with the O^{2-} terminations concentration (evaluated from the C-Ti-O(ii) peak areas) being relatively higher for the $Ti_3C_2T_x$-LiF sample and the OH^- terminations concentration (evaluated from the C-Ti-OH peak areas) being relatively higher for the $Ti_3C_2T_x$-HF sample. The surface oxides concentration (evaluated from the O^{2-} peak area) was also higher for the $Ti_3C_2T_x$-LiF sample. The average titanium oxidation state of the $Ti_3C_2T_x$-LiF sample was slightly higher for the $Ti_3C_2T_x$-HF sample, +2.5 and +2.3, respectively (evaluated from the Ti2p regions). Therefore, it was concluded that the $Ti_3C_2T_x$-LiF sample in its initial
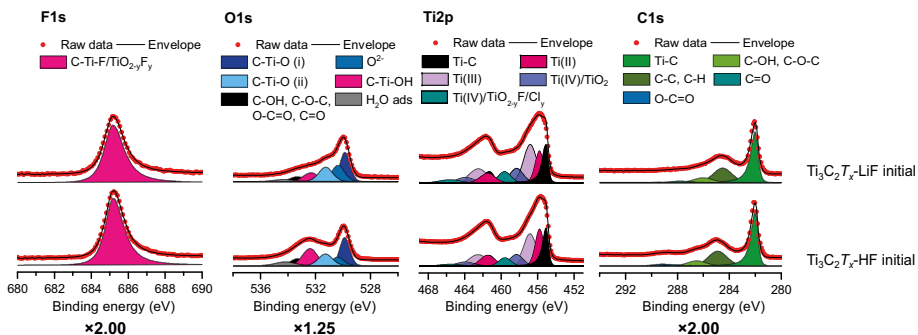
Figure 4.11. The F1s, Ti2p, O1s and C1s regions for the $Ti_3C_2T_x$-LiF and $Ti_3C_2T_x$-HF films in their initial states. The F1s, O1s and C1s spectra were normalised by the highest raw data point in the corresponding Ti2p spectra. The number at the bottom indicates the magnification that was used for the spectra representation.

state was on average slightly more oxidised in comparison with the $Ti_3C_2T_x$-HF sample.

The electrochemical data obtained in LIB cells, however, looked very different for the samples. The cyclic voltammograms for the $Ti_3C_2T_x$-LiF electrode showed relatively larger oxidation and reduction currents compared to those for the $Ti_3C_2T_x$-HF electrode and also showed capacity activation, *Figure 4.12A*.
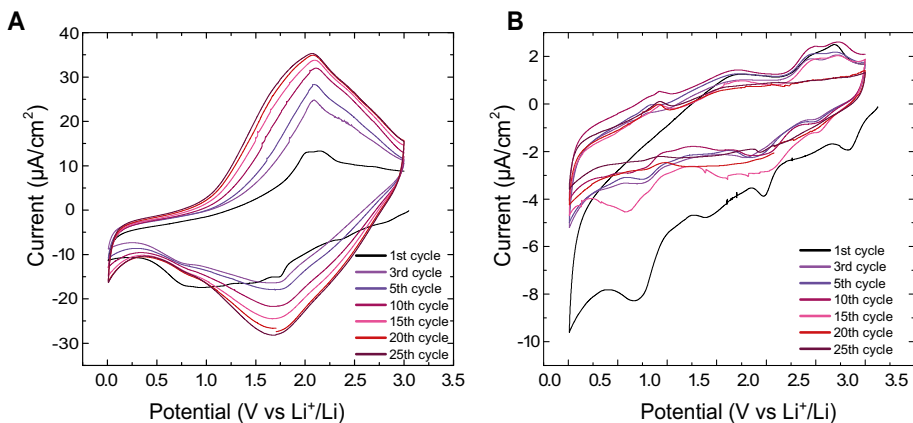
Figure 4.12. Cyclic voltammograms recorded at the rate of 0.1 mV s^{-1} between 0.01 and 3 V vs. Li$^+$/Li for a $Ti_3C_2T_x$-LiF(**A**) and a $Ti_3C_2T_x$-HF(**B**) electrode in their states.

On the contrary, the cyclic voltammograms recorded for the $Ti_3C_2T_x$-HF electrode showed signs of a double layer charging as well as incomplete oxidation, as the reduction charge (area below 0 μA/cm^2) was much larger than the corresponding oxidation charge (area above 0 μA/cm^2), *Figure 4.12B*.

The different electrochemical behaviours of the $Ti_3C_2T_x$ films, which had similar average titanium oxidation states on the surface can therefore be explained by different degrees of sample oxidation in the bulk. One can, however, not exclude different degrees of $Ti_3C_2T_x$ sheet restacking during the synthesis procedures.

How were the surfaces of the initial $Ti_3C_2T_x$-LiF and $Ti_3C_2T_x$-HF films altered during the heat treatment? The evolution of the F1s, O1s, Ti2p and C1s XPS spectra during heating from room temperature to 775 °C for the $Ti_3C_2T_x$-LiF and $Ti_3C_2T_x$-HF films can be seen in *Figure 4.13*.

Analysis of the spectra showed that both of the films featured a decrease in the C-Ti-F/$TiO_{2-y}F_y$ peak in the F1s region (a similar defluorination process has also been reported before [115]), a decrease in the Cl2p peak (seen from the survey spectra) an evolution of species in the O1s region, subtle changes in the Ti2p region and no considerable changes in the C1s region (except for a decrease in the peaks that were attributed to adventitious species such as O-C=O, C=O, C-OH, C-O-C and C-C, C-H). The changes in the O1s and Ti2p spectra can be best tracked from their fittings in *Figures 4.14 A* and *B* for selected temperatures.

For both the $Ti_3C_2T_x$-LiF and $Ti_3C_2T_x$-HF films no significant change in the average titanium oxidation state was noticed. For the $Ti_3C_2T_x$-LiF sample, the increase was from +2.46 to +2.51 and the value remained the same after cooling to RT in the analyser chamber. For the $Ti_3C_2T_x$-HF sample, the increase was from +2.32 to +2.40 and the value decreased to the original value after cooling to RT in the analyser chamber.

The O1s spectra show a progressive decrease in the C-Ti-O(i) (oxygen bridging two Ti sites) relative peak area and an increase in the relative area of the C-Ti-O(ii) (oxygen double bonded to Ti) peak as well as in that of the O^{2-} peak which was less prominent in the $Ti_3C_2T_x$-HF case. This can be interpreted as the surface oxides O^{2-} species were formed during the heating. It can be speculated that these are Ti_xO_y phases, containing mainly Ti(II) and Ti(III) oxidation states.

The surface changes during the heating were hence ascribed to the i) increase in the surface oxides concentration and the O^{2-} termination groups, ii) decrease in the concentration of the OH^- and the oxygen bridging two Ti sites termination groups, iii) partial elimination of the F^- and Cl^- termination groups.

The in situ XPS heat treatment experiment was repeated but this time the procedure also included an air exposure step for 5 minutes after the heating. The air exposure step was added to promote the surface termination group substitution yielding O^{2-} terminations, since O-terminated MXenes are believed to show better electrochemical capacities [65, 116, 126, 127]. The in situ XPS heat treatment data for the RT films before and after heating and exposure to air are shown in *Figure 4.14 C* and *D*.
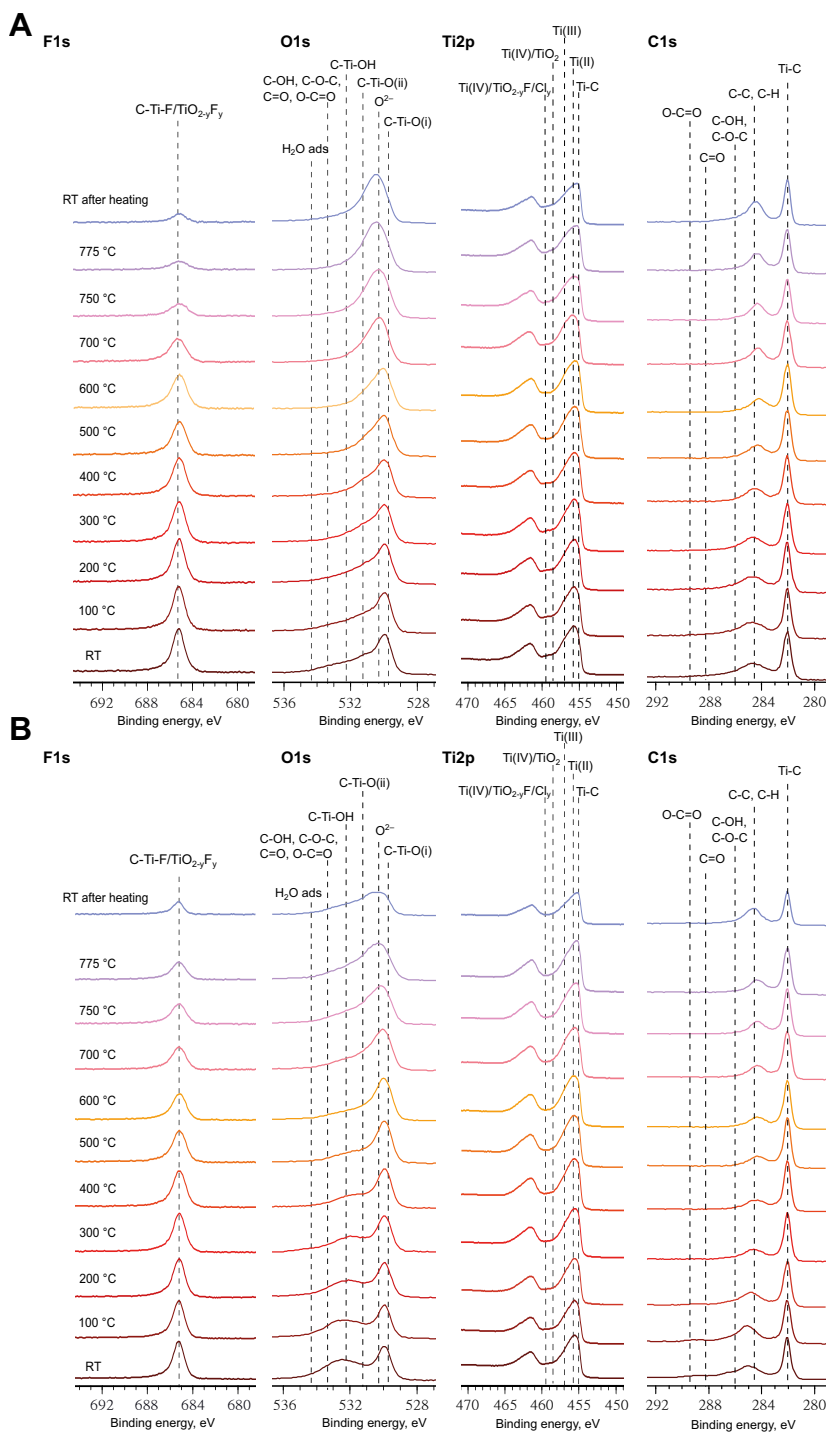
48

Figure 4.13. The F1s, Ti2p, O1s and C1s regions for the **A**: $Ti_3C_2T_x$-LiF and **B**: $Ti_3C_2T_x$-HF film that underwent in situ XPS heating.
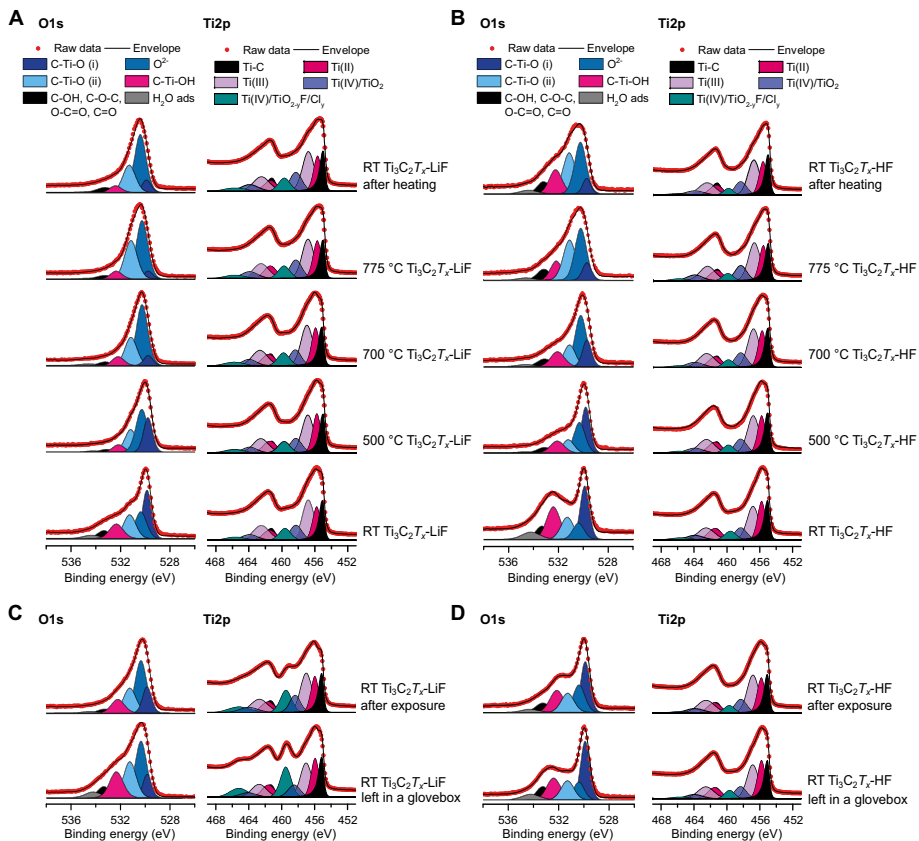
Figure 4.14. The Ti2p and O1s regions for the $Ti_3C_2T_x$-LiF(**A**) and the $Ti_3C_2T_x$-HF(**B**) films recorded at room temperature (RT), after heating to 500, 700 and 775 °C as well as after the cooling down. The Ti2p and O1s regions for analogous $Ti_3C_2T_x$-LiF(**C**) and the $Ti_3C_2T_x$-HF(**D**) films which were left in a glovebox for 6 months and underwent heat treatment to 700 °C followed by an air exposure step.

The major changes that were seen after the experiment with an air exposure step compared to the heating experiment without one included a relatively higher amount of OH^- and C-Ti-O(i), bridging oxygen, terminations as well as less of the O^{2-} surface oxide species and C-Ti-O(ii), double bonded oxygen terminations, seen for both of the $Ti_3C_2T_x$-LiF and $Ti_3C_2T_x$-HF samples. It was therefore concluded, that other post-heating procedures should be used to more efficiently substitute the termination groups of $Ti_3C_2T_x$ to predominantly O^{2-}.

The average titanium oxidation state of the $Ti_3C_2T_x$-HF film increased from +2.31 to +2.36, as well as that there was a relatively higher increase in the surface oxides concentration, see *Figure 4.14D*. A similar analysis for the $Ti_3C_2T_x$-LiF film (*Figure 4.14C*) showed that the average titanium oxidation state had remained the same before and after the heat treatment and air ex-

posure, +2.6, which is comparatively higher than that for the heated and air exposed $Ti_3C_2T_x$-HF sample, but also higher than that for the similar film used in the heating experiment mentioned above.

How did these surface changes affect cycling? As predicted, the heat treatment and air exposure improved the capacity of the films, as can be directly evidenced from *Figure 4.15*.
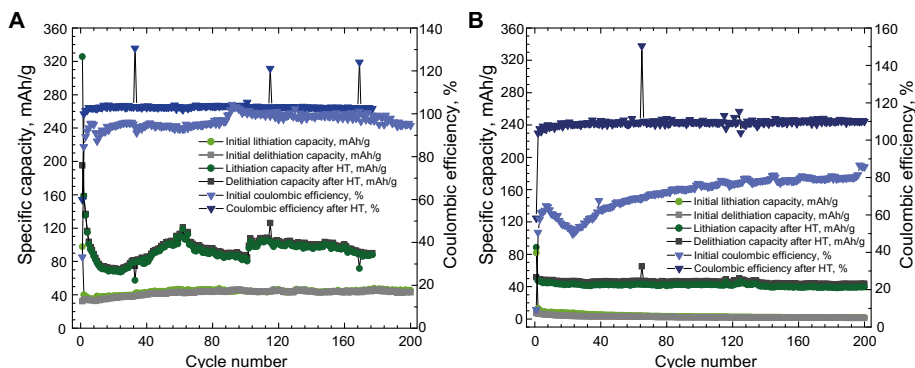

Figure 4.15. The lithiation and delithiation capacities as well as the coulombic efficiency as a function of the cycle number for the freestanding $Ti_3C_2T_x$-LiF(**A**) and $Ti_3C_2T_x$-HF(**B**) electrodes that underwent in situ XPS heating to 700 °C coupled with subsequent air exposure and CC cycling with a current density of 10 mA g^{-1} from 0.01 to 3 V vs. Li^+/Li.

The $Ti_3C_2T_x$-LiF capacity was increased from the previously seen ~40 mAh g^{-1} for the electrode in its initial state to ~80 mAh g^{-1} after 160 cycles, while the coulombic efficiency after the heat treatment stayed at 102-103% during the cycling, as one can see in *Figure 4.15A*. The capacity for the $Ti_3C_2T_x$-HF electrode was stabilised at ~40 mAh g^{-1} after 200 cycles while the initial capacity was ~5 mAh g^{-1}, *Figure 4.15B*. One can also observe that coulombic efficiency values of 110% were seen during the cycling. This means that the oxidation capacity was higher than the reduction capacity and the activation of the material was ongoing for both $Ti_3C_2T_x$-LiF and $Ti_3C_2T_x$-HF after the heating. Therefore, heat treatment can be considered as a post-synthesis treatment resulting in an improvement of the electrochemical cycling of $Ti_3C_2T_x$ electrode which, however, does not suppress the capacity activation seen during the cycling.

The XPS data for the samples that were measured before the heating followed by an air exposure step show that the surfaces of the $Ti_3C_2T_x$-LiF and $Ti_3C_2T_x$-HF samples were altered to some extent upon storage in a glovebox for 6 months compared to the samples in their initial states (freshly prepared). The most pronounced difference is the increase of TiO_{2-y}F/Cl_y peak in the Ti2p region, compare *Figure 4.14 A* and *C*. This raises a question about the influence of $Ti_3C_2T_x$ sample storage in an initial state on capacity activation. The cyclic voltammograms recorded for the $Ti_3C_2T_x$-LiF and $Ti_3C_2T_x$-HF

electrodes that were stored in their initial states in a glovebox for 10 months both showed capacity activation, *Figure 4.16*. Owing to the fact that the samples were left non-dried in the oxygen-poor environment, it is assumed that the water trapped in the electrodes enabled titanium species oxidation in the $Ti_3C_2T_x$ electrodes which resulted in pronounced capacity activation. The CC data also indicated an increase in the capacity on cycling which was rather similar for both samples, from ~30 mAh g^{-1} on the second cycle to ~55 and ~60 mAh g^{-1} on the 95th cycle, for the $Ti_3C_2T_x$-HF and $Ti_3C_2T_x$-LiF samples, respectively.
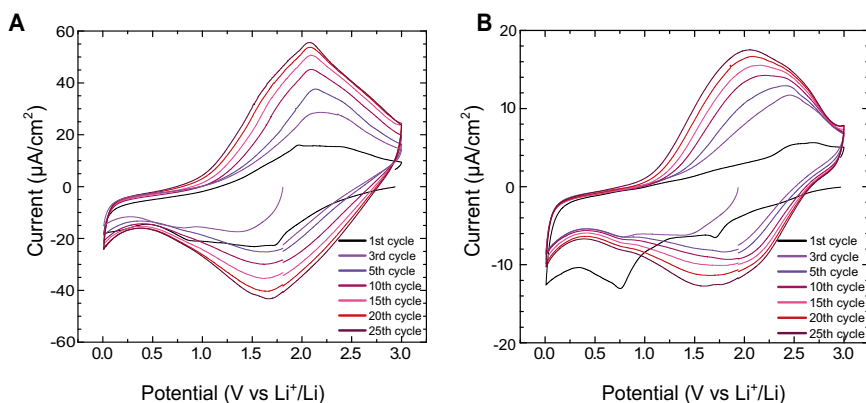
Figure 4.16. Cyclic voltammograms recorded at the rate of 0.1 mV s^{-1} between 0.01 and 3 V vs. Li$^+$/Li for a $Ti_3C_2T_x$-LiF(**A**) and for a $Ti_3C_2T_x$-HF(**B**) electrodes which were left in a glovebox for 10 months in their non-dried states.

Therefore, the higher capacities seen after the heating were attributed to the higher concentrations of the Ti_xO_y species for both samples. As the difference in the average titanium oxidation state within several nanometers depth (the depth of XPS analysis) for the $Ti_3C_2T_x$-LiF and $Ti_3C_2T_x$-HF samples after heating and air exposure was small, it is reasonable to assume that the electrodes differed with respect to their structure and the average titanium oxidation state in the bulk. This could be explained by different degrees of the oxidation and restacking of the flakes for $Ti_3C_2T_x$-LiF and $Ti_3C_2T_x$-HF films, not only before, but also after heating. It is concluded that the $Ti_3C_2T_x$-HF electrode was relatively less oxidised and had a more compact structure than the $Ti_3C_2T_x$-LiF electrode. When samples were left in a glovebox for 10 months both of them underwent further oxidation and showed capacity activation during cycling. This finding suggests that that the $Ti_3C_2T_x$ was already activated before the heat treatment and in the absence of the heat treatment more cycles were needed to get the $Ti_3C_2T_x$ sample activated.

4.2 *A*-site cation deficient perovskite oxide Li018STN as a negative electrode in lithium-ion batteries

As was already mentioned in the introduction, over-lithiation of the perovskite oxide Li018STN is defined as the insertion of more than one lithium ion per available *A*-site. Before proceeding with the main findings of **Paper IV**, it is practical to clarify how many vacant *A*-sites there are in the structure, what is the lithium occupancy within the vacancy and what are the oxidation states of ions in the as-synthesised L018STN.

Since in Li018STN the *A*-site is occupied by 0.66 Sr^{2+} per formula unit, then the number of vacancies, or □, is: 1 - 0.66 = 0.34. However, 0.18 mol of Li^+ is already incorporated into the structure to maintain the electroneutrality, therefore the number of the remaining vacant *A*-sites is 1 - 0.66 - 0.18 = 0.26 per formula unit. The lithium occupancy of the *A*-site vacancy in the pristine L018STN is then: $\frac{0.18}{0.34}$ = 0.53, meaning that only half of *A*-site vacancies are occupied by Li^+.

The electroneutrality of the compound is established only if titanium has an oxidation state of +4 and niobium has an oxidation state of +5: 0.18 × (+1) + 0.66 × (+2) + 0.5 × (+4) + 0.5 × (+5) + 3 × (-2) = 0.18 + 1.32 + 2 + 2.5 - 6 = 0.

4.2.1 Redox activity of L018STN in LIBs

The reduction of titanium and/or niobium to lower oxidation states than IV and V, respectively, is then expected on electrochemical cycling, resulting in the insertion of more than 0.18 mol of Li^+ into the Li018STN structure, or *x* of Li^+ in $Li_{0.18+x}Sr_{0.66}Ti_{0.5}Nb_{0.5}O_3$.

Cyclic voltammograms recorded for a L018STN/Li cell from 0.25 to 2.5 V vs. Li^+/Li, *Figure 4.17A*, reveals two pairs of redox peaks at 1.6-1.8 V and 1.2-1.4 V vs. Li^+/Li. This indicates that at least two redox reactions are responsible for the electrochemical cycling of L018STN.

Among the redox reactions responsible for the electrochemical capacity of L018STN in the selected potential window (0.25 – 3 V vs. Li^+/Li), the most probable should include the redox couples Nb(V)/Nb(IV), Nb(IV)/Nb(III) and Ti(IV)/Ti(III). Based on the literature data, the redox peak couple observed at 1.6-1.8 V vs. Li^+/Li can be ascribed to the Nb(V)/Nb(IV) redox couple, similar to what was reported for Nb_2O_5 [128–130] and $Ln_{1/3}NbO_3$, where *Ln* = La, Nd [131]. While the redox peaks at 1.2-1.4 V vs. Li^+/Li can stem from the Ti(IV)/Ti(III) redox couple, based on the reports for LLTO [132–134]. The Nb(IV)/Nb(III) reduction and oxidation peaks should appear at about 1.3 V vs. Li^+/Li [128], however such a redox reaction was not detected with XPS.

XPS on L018STN electrodes cycled to various lithiation and delithiation states on the first cycle was employed to investigate the redox active species in L018STN, *Figure 4.18A*. The data indicate that both niobium and titanium
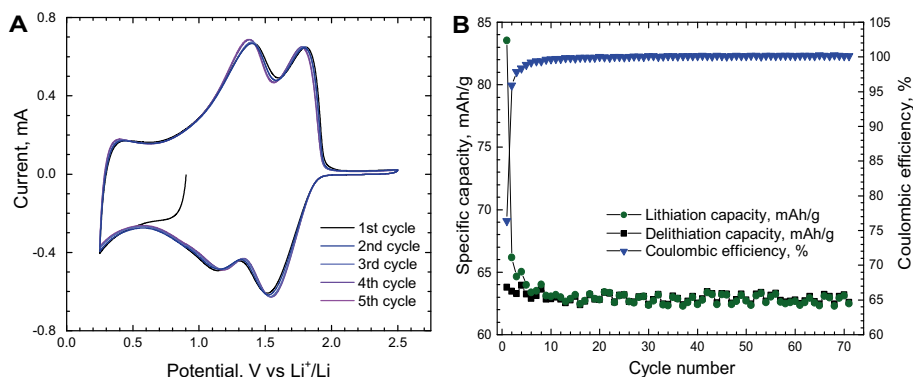
Figure 4.17. **A**: Cyclic voltammograms recorded at a scan rate of 0.5 mV s^{-1} from 0.25 to 2.5 V vs. Li$^+$/Li for a pristine L018STN electrode. **B**: Lithiation (reduction) and delithiation (oxidation) capacities extracted from the CC cycling at 0.1 mA cm^{-2} from 0.25 to 3 V vs. Li$^+$/Li as a function of the cycle number for a similar electrode.

were redox active on cycling, partial reduction from Nb(V) to Nb(IV) and from Ti(IV) to Ti(III) on lithiation and reversible oxidation back to Nb(V) and Ti(IV) on delithiation was detected. Hence, it is concluded that the energy storage mechanism was Faradic. Based on the XPS analysis, however, it was not possible to distinguish which of the redox reactions takes place first, see *Figure 4.18B*.

Analysis of the CC cycling between 0.25 and 3 V vs. Li$^+$/Li showed stable cycling with lithiation (reduction) and delithiation (oxidation) capacities of about 63 mAh g^{-1} and a coulombic efficiency close to 100% on the fifth and subsequent cycles, corresponding to the reversible redox reactions coupled with insertion/deinsertion of 0.42 Li$^+$ per formula unit (x), *Figure 4.17B*. The lithium occupancy of the *A*-site vacancy in the Li$_{0.18+0.42}$Sr$_{0.66}$Ti$_{0.5}$Nb$_{0.5}$O$_3$ is then: $\frac{0.6}{0.34} = 1.76$.

From a structural point of view, it is assumed that up to two lithium ions can occupy each *A*-site cavity, or 0.5 Li$^+$ (x) per formula unit. If this is the case, the reduction of titanium and niobium would result in capacity of 75.5 mAh g^{-1}. Therefore, 84% of the maximum capacity was reached on cycling to 0.25 V vs. Li$^+$/Li.

The initial capacity loss observed on the first four cycles was about 20 mAh g^{-1}. Calculations, done in a similar way as was described in **Paper I**, show that the formation of a 20 nm thick SEI layer on the surface of a 13 mm in diameter L018STN electrode would require a charge of about 7 mAh g^{-1}. Therefore, as in the Ti$_3$C$_2T_x$ electrode case, only 35% of the observed capacity loss cycle could be attributed to the SEI formation. Similarly, even in the case of the L018STN electrode, the source of the remaining 65% of irreversible capacity could be the reduction of water adsorbed on the surface of the L018STN electrode. A water content as low as 31 μg per electrode, or 0.42 wt.% (calculated
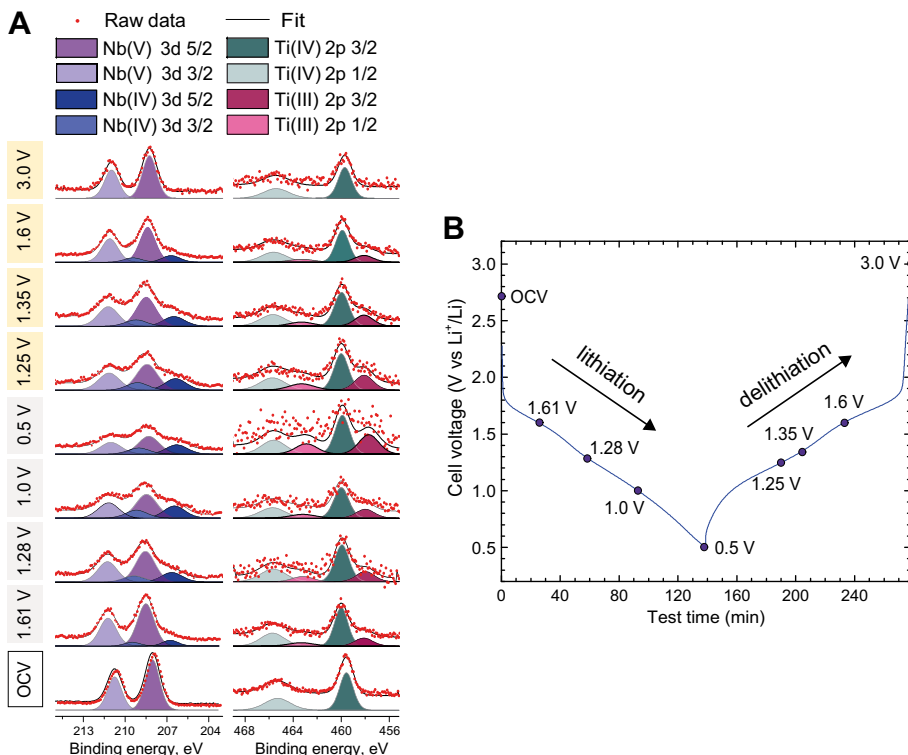
Figure 4.18. **A**: Nb3d and Ti2p spectra of the L018STN electrodes extracted from the cells on lithiation (grey) and delithiation (yellow) within the first cycle as well as from the cell that was rested at the OCV (about 2.7 V vs. Li^+/Li). Evolution as a function of the state of charge. **B**: CC cycling curve for a L018STN/Li cell cycled on the first cycle at 0.1 mA cm^{-2} between 0.5 and 3 V vs. Li^+/Li showing the potentials at which the cells were stopped and the electrodes were extracted for an XPS analysis.

for the active mass of L018STN in the electrode used for the ICI cycling, 7.296 mg) would be sufficient to explain this.

4.2.2 Lithium-ion diffusion inside the LSTN structure on lithiation and over-lithiation

Paper IV also explores the crystallographic positions of Li^+ in the pristine and over-lithiated LSTN material and suggests possible diffusion paths for Li ions on lithiation and over-lithiation.

Neutron diffraction data for the as-synthesised L018STN sample measured at 6 K revealed two positions for Li^+ in the structure. The positions are Li1: 6f (0.5, 0.5, 0.15) lying offset from the oxygen window (a four oxygen coordinated site), reported previously [135], and Li2: 8g (0.29 0.29 0.29), near the Ti/NbO_6 octahedral face and coordinated by three oxygen atoms. At room tem-

perature, Li^+ is predominantly found on the 6f site with fast hopping between the 6f positions via the 8g site. These conclusions are supported by NMR measurements and AIMD simulations.
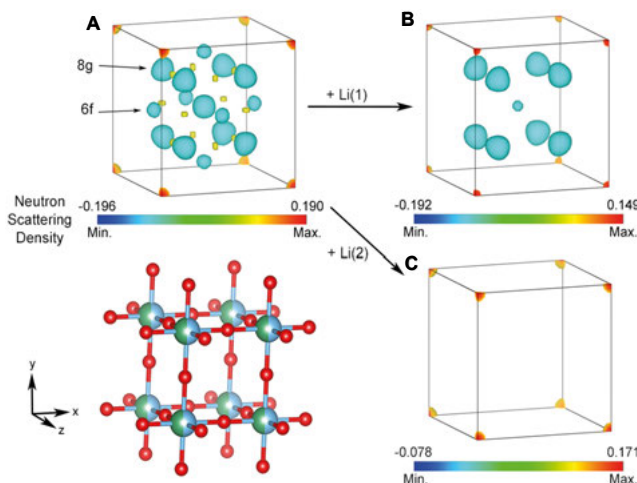
Figure 4.19. Fourier difference maps before (**A**) and after including lithium in the L018STN model on the Li1(6f, **B**) and Li2(8g, **C**) positions, respectively. An intensity cut-off of 0.12 was used in every case to remove low-intensity noise. A picture of the structure of an *A*-site is provided for reference.

A previous operando neutron diffraction data analysis for an LSTN sample lithiated to 1 V [136] show that the O_4 window centre, or the 3c (0.5, 0.5, 0) site, becomes more accessible and energetically favourable for Li^+ in the lithiated state. A study employing X-ray diffraction revealed the existence of two cubic perovskite phases on lithiation, one more lithiated than the other [135]. This phase segregation was explained by electrostatic repulsion between neighbouring lithium ions on insertion of more than one Li^+ per vacant site which led to the increased bulk resistance. ICI measurements on CC cycling were therefore performed to explore the possibility of phase segregation due to the loss of lithium-ion mobility.

The ICI results presented in *Figure 4.20* show that the lithium-ion mobility ($m_{Li}+$) on the second lithiation decreases by roughly half an order of magnitude when $\sim$0.25 Li^+ per formula unit is inserted (average *A*-site occupancy of 1.26 Li^+), reaching a minimum at 0.34-0.36 Li^+ per formula unit (average *A*-site occupancy of $\sim$1.56 Li). This decrease in lithium-ion mobility on lithiation step becomes less noticeable after extensive cycling and is not detected during the delithiation processes. In contrast, at the beginning of delithiation step the lithium-ion mobility is an order of magnitude higher. This observation supports the hypothesis that resistance to diffusion increases during insertion beyond 1 Li^+ per vacant site due to electrostatic repulsion and facilitates the delithiation which is reflected in the high mobility of lithium ions at the begin-
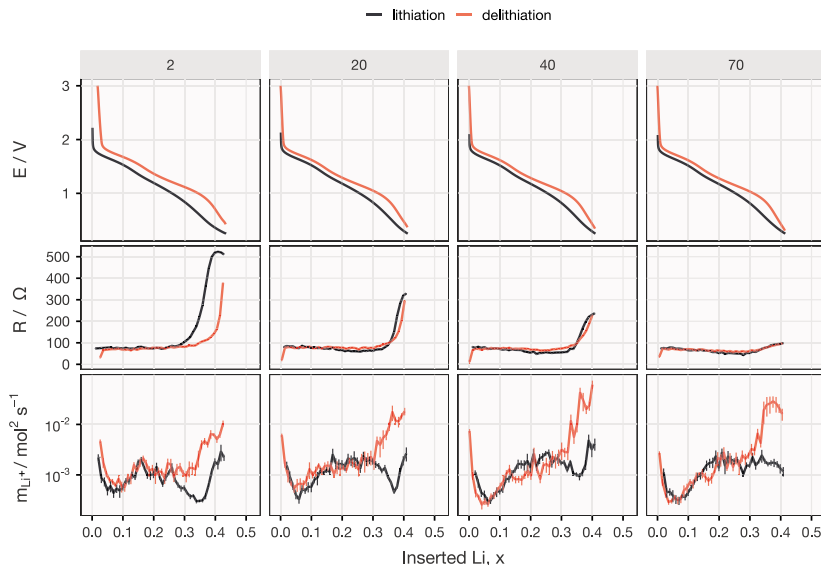
Figure 4.20. The potential (E), internal resistance (R), and lithium-ion mobility ($m_{Li}+$) plotted against inserted Li$^+$ content (x) in Li$_{0.18+x}$Sr$_{0.66}$Ti$_{0.5}$Nb$_{0.5}$O$_3$ for the cycles 2, 20, 40 and 70 (indicated on top of the figure with numerals) measured during the CC cycling coupled with ICI of L018STN/Li cell in 1 M LiPF$_6$ in 1:1 vol EC:DEC.

ning of the delithiation step. The most unexpected feature of the ICI results is the restoration of lithium-ion mobility on lithiation step at ∼0.4 Li$^+$ per formula unit (average *A*-site occupancy of 1.71 Li). Such unusual behaviour could be explained by the subtle LSTN structure adjustments to the high lithium concentration. On insertion of more than one Li$^+$ per vacant *A*-site the LSTN structure rearranges to maximise the distance between mobile lithium ions and minimise the electrostatic repulsion within the *A*-site cavity. When minimising electrostatic repulsion is no longer possible, the lithium-ion mobility subsequently drops, i.e., at an occupancy of ∼1.56 Li. However, at the average *A*-site occupancy of 1.71 Li on reduction it is suggested that the O$_4$ window expands due to Ti/Nb-O bond length increase and lithium is forced into the O$_4$ window (0.5 0.5 0) site. This shift of Li$^+$ position modifies the diffusion behaviour from site percolation (*Figure 1.5A*) to bond percolation (*Figure 1.5B*).

The 0.18 mol of Li$^+$ that were never extracted from Li018STN were assumed to become pinned in the O$_4$ window over time to maintain the bond percolation diffusion at the end of the delithiation step. This reasoning could explain the fact that lithium-ion mobility loss on lithiation was no longer observed as well as the internal resistance of the cell considerably decreased at the end of the lithiation step after 70 cycles.

5. Conclusions and outlook

This thesis work focuses on the study of freestanding 5-7 µm thick $Ti_3C_2T_x$ MXene films and polycrystalline A-site deficient $Li_{0.18}Sr_{0.66}Ti_{0.5}Nb_{0.5}O_3$ (L018STN) perovskite oxide composite electrodes as negative electrodes for lithium- and sodium-ion batteries.

The results for $Ti_3C_2T_x$ electrodes demonstrate that the charge storage mechanism is based on redox reactions involving the Ti(I), Ti(II), Ti(III), and Ti(IV) species in the surface Tx-Ti-C layer of the $Ti_3C_2T_x$. The Ti-C layer of the $Ti_3C_2T_x$, is, however, electrochemically inactive. Furthermore, the restacking of the individual flakes within the bulk of the $Ti_3C_2T_x$ electrode decreases the electroactive surface area of the freestanding $Ti_3C_2T_x$ electrode available for the redox reactions.

The variation in the capacities reported for the material in the literature is in this work explained by the various degrees of titanium oxidation obtained during the electrode manufacture and pretreatment procedures. The initial cycles for a $Ti_3C_2T_x$ electrode in a LIB reveal the presence of a significant irreversible capacity, which predominantly is due to the reduction of the water adsorbed on the surface of the $Ti_3C_2T_x$ electrode and confined between $Ti_3C_2T_x$ flakes in the freestanding electrode.

The capacity activation seen for $Ti_3C_2T_x$ electrodes during cycling in LIBs and SIBs is attributed to the gradual oxidation of the surface titanium species to higher oxidation states. It is anticipated that the water confined between the $Ti_3C_2T_x$ flakes can facilitate this oxidation. Furthermore, according to the results presented here, it is possible to increase the capacities of $Ti_3C_2T_x$ electrodes further by oxidation of the titanium surface species using heat treatment. The synthesis routes affect the degrees of oxidation and restacking of the individual flakes in $Ti_3C_2T_x$ electrodes and hence their reversible capacities.

Based on these findings, it is concluded that $Ti_3C_2T_x$ MXene cannot be considered as promising negative electrode material for lithium- and sodium-ion systems due to its limited redox activity, which typically does not involve the entire bulk of the freestanding electrodes. This limitation comes directly from the structure of the $Ti_3C_2T_x$ flake and the 2D nature of the material. The assembly of 2D flakes into a 3D structure is inevitable for the realisation of real-world applications, including battery electrodes. In such cases, the properties of single flakes may, however, not be seen for a multilayered structure. A comparison of the $Ti_3C_2T_x$ electrochemical behavior with that of TiO_2 shows that higher capacities can be obtained with TiO_2 electrodes.

This thesis work also examines the electrochemical behavior of another titanium-based battery material, the *A*-site deficient Li018STN perovskite oxide shedding light on the capacity origin and lithium-ion diffusion mechanisms before and after over-lithiation. Based on the findings, the design of *A*-site cation deficient perovskite oxides oxides with Li^+ in the *A*-site window could prove to be a feasible strategy to obtain higher mobilities and cycling stabilities for *A*-site cation deficient perovskite oxides oxide electrodes. Further fundamental investigations of the redox activities of niobium and titanium are proposed as a way to realise higher energy densities for perovskite oxide electrodes.

Finally, the thesis work emphasises the significance of employing a multi-technique approach to attain a good understanding of the underlying redox mechanisms when analysing battery materials. For example, the analysis of the results for two $Ti_3C_2T_x$ films, manufactured using two different synthesis methods, showed that the XPS-based titanium oxidation states on the surface of the films did not represent the bulk oxidation states. XAS was found to be a powerful complementary technique to XPS as XAS was able to reveal the presence of redox-active titanium species also in the bulk of the electrodes. An even better picture of the differences between the electrodes was obtained with cyclic voltammetry as the electrochemical results depended on the electrochemically active material present in the entire electrodes. Additionally, it was only through the use of a combination of electrochemical, computational, and diffraction techniques that a better understanding of the lithium-ion diffusion paths within the LSTN structure could be obtained.

6. Populärvetenskaplig sammanfattning

Litiumjonbatterier har en stor betydelse i vårt dagliga liv. Inte bara för att de som lagringsenheter med hög energitäthet gör att det mesta av vår elektronik är portabel, utan också för att de möjliggör energilagringslösningar för förnybara energikällor som varierar i tid som till exempel solstrålning, vind och vattenrörelser. Det moderna samhällets behov av bättre batterier är den främsta drivkraften för forskningen om litiumjonbatterier. Batteriforskare uppmanas att utveckla nya material och främja förståelsen av elektrokemiska processer för att göra litiumjonbatterier billigare, säkrare, lättare och mer hållbara.

Ett litiumjonbatteri är en enhet som lagrar kemisk energi genom redoxreaktioner och omvandlar den till elektrisk energi. Ett litiumjonbatteri består av två elektroder, en negativ och en positiv elektrod, som skiljs åt av en separator och en elektrolyt. Vid urladdning sker en oxidationsreaktion vid den negativa elektroden varvid elektroner och litiumjoner bildas. Dessa rör sig sedan till den positiva elektroden där en reduktionsreaktion sker. Elektronerna färdas genom en yttre krets och skapar den elektriska strömmen, medan litiumjonerna transporteras genom elektrolyten och separatorn för att kompensera för laddningsöverföringen i den yttre kretsen. Vid uppladdning, när strömmen tillförs systemet, sker det motsatta. Natriumjonbatterier fungerar enligt samma princip som litiumjonbatterier men använder istället natriumjoner som laddningsbärare.

Kommersiella litiumjonbatterier utnyttjar grafit som en negativ elektrod samt litium-nickel-mangan-koboltoxider, $LiNi_xMn_yCo_zO_2$ ($x + y + z = 1$), eller litium-järnfosfat, $LiFePO_4$, som en positiv elektrod. Elektroder som används i kommersiella batterier är ofta kompositelektroder gjorda av redoxaktivt material blandat med ett ledande tillsatsmedel som binds till en strömsamlare med hjälp av ett bindemedel. Separatorerna är vanligtvis gjorda av polyeten och polypropen eller keramiska material, medan elektrolyten vanligtvis är ett litiumsalt löst i en blandning av organiska lösningsmedel, även innehållande med en liten mängd av en rad olika tillsatser som förbättrar batteriernas prestanda.

Forskningen om negativa elektroder fokuserar, till exempel, på att lösa säkerhetsproblem som är förknippade med dendrittillväxt som kan leda till en kortslutning av batterier vid höga cyklingshastigheter, irreversibla processer inuti elektrodmaterialet och sätt att förbättra den långvariga cyklingstabiliteten. För att undvika dessa problem kan ett material med partiklar i nanostorlek med kort litiumjondiffusionslängd, pseudokapacitivt beteende och hög strukturell integritet under elektrokemisk cykling vara av intresse. Ett exempel på ett sådant

material är en nyligen upptäckt klass av tvådimensionella (2D) material som kallas MXener.

MXener är en familj av 2D övergångsmetallkarbider och nitrider som produceras från MAX-faser (där M är en övergångsmetall, A är ett A-gruppselement och X är N och/eller C) genom att kemiskt avlägsna A-skikten (t.ex. Al). MXener har den allmänna formeln $M_{n+1}X_nT_x$ där n = 1 – 4, T är ytgrupper (t.ex., =O, -OH, -F eller -Cl) och $x \leq 2$. Ett enda lager av $Ti_3C_2T_x$, den hittills mest studerade medlemmen av MXene-familjen, är cirka 11 Å tjockt. Detta lager har en elektroniskt ledande Ti-C kärna som omges av två redoxaktiva T_x-Ti-C lager.

I den här avhandlingen studerades fristående $Ti_3C_2T_x$ elektroder (som inte innehöll bindemedel eller ledande tillsatsmedel) i litium- och natriumjonbatterier. Redan tidigt i studierna konstaterades det att kapaciteten hos $Ti_3C_2T_x$-elektroderna var ganska låg på grund av att titanets oxidationstal i $Ti_3C_2T_x$ var ganska lågt. Titanet i Ti-C-kärnskiktet av $Ti_3C_2T_x$ visade sig vara redox-inaktivt och redoxreaktionerna som involverade Ti(II), Ti(III) och Ti(IV) i T_x-Ti-C-skiktet gav upphov till de observerade kapaciteterna. Vidare visades det också sig att oxidationen av $Ti_3C_2T_x$-flingor i närvaro av luft och vatten leder till en ökning av det genomsnittliga oxidationstalet för titan in $Ti_3C_2T_x$-elektroderna. Denna oxidation leder ytterst till bildandet av TiO_2. Därför drogs slutsatsen att beroende på förhållandena under syntesen och tillverkningen av $Ti_3C_2T_x$-elektroderna i luft- och vattenmiljö, så kommer titanet i T_x-Ti-C att oxideras i olika grad. Detta skulle förklara de olika kapaciteterna som observerats för materialet vid elektrokemisk cykling. Vatten som adsorberats på ytan och som är instängt mellan $Ti_3C_2T_x$-lagren i en fristående $Ti_3C_2T_x$-elektrod visade sig förklara den irreversibla kapaciteten som sågs under de första cyklerna för litiumjonbatterierna.

$Ti_3C_2T_x$-elektrodernas kapacitet visade sig öka med antalet cykler, när $Ti_3C_2T_x$/Li- och $Ti_3C_2T_x$/Na-celler cyklades mer än tvåhundra cykler, vilket är ganska ovanligt för en elektrokemisk cell. Fenomenet bakom denna kapacitetsaktivering tillskrevs en gradvis oxidation av titan i ytskiktet av T_x-Ti-C till Ti(III) och Ti(IV) vid elektrokemisk cykling.

Värmebehandlingsexperiment visade att det är möjligt att förbättra $Ti_3C_2T_x$-elektrodernas kapacitet genom att värma dem till 700 °C i en vakuumkammare. Denna behandling resulterar i en förlust av F^- och Cl^- ytgrupper samt en oxidation av titanet i $Ti_3C_2T_x$ till titanoxid faser Ti_xO_y.

På basis av resultaten drogs slutsatsen att $Ti_3C_2T_x$ MXener inte kan anses lovande som negativa elektroder för litium- och sodiumjonbatterier på grund av att deras redoxaktivitet är ganska begränsad. En jämförelse av den elektrokemiska prestandan för $Ti_3C_2T_x$-elektroder med de för elektroder bestående av nanotuber av titandioxid och titandioxid-nanopartiklar i natrium-jonbatterier visade att $Ti_3C_2T_x$-elektroderna inte kunde konkurrera med titan-dioxidelektroderna i natrium-jonbatterier.

Forskningen på A-plats fattig perovskitoxid $Li_{0.18}Sr_{0.66}Ti_{0.5}Nb_{0.5}O_3$ (Li018STN), ett annat Ti-baserat batterimaterial som studerats i den här avhandlingen, visade att den användbara litierings- och delitieringskapaciteten hos Li018STN härrörde från Nb(IV)/Nb(V) och Ti(III)/Ti(IV) redoxreaktioner.

Elektrokemisk cykling av Li018STN visade att det är praktiskt möjligt att infoga mer än $1\,Li^+$ per A-plats. Detta fenomen kallas "överlitiering". Förändringen i litiumjonmobilitet som observerades för Li018STN vid överlitiering antogs vara orsakad av ändring i litiumjondiffusionsbeteendet från platsperkolering till bindningsperkolering. De erhållna resultaten ger värdefulla insikter rörande de kemiska drivkrafterna som möjliggör erhållandet av högre kapaciteter och förbättrad diffusion i A-plats fattiga perovskitoxider.

7. Acknowledgments

I would like to thank my main supervisor, Kristina Edström, for giving me this opportunity to work at Ångström Laboratory in the Structural chemistry group. Thank you for letting me grow and develop my skills as well as for all the encouragement and appreciation I have received during the journey. I am filled with gratitude to say I was co-supervised by Leif Nyholm. Thank you for all the provided support, constructive feedback and discussions. Thanks to you amongst my weaponry I have such diverse elements as rough estimations, the ability to use chain argument and invulnerability to reviewers' comments. Big thanks go to my other co-supervisor, Maria Hahlin. Thank you for all the fruitful discussions around my spectroscopy results, where not only we scratched the surface, but also went in-depth and into detail.

I would also like to thank Johanna Rosén for managing and funding this project and all of my co-authors: Joseph Halim, William Brant, Andoria Kotronia, Charlotte Ihrfors, Yu-Chuan Chien, Tove Ericson. Joseph thank you for all provided help on the XPS analysis of MXenes and your suspensions, my work would not be possible without your syntheses. Will, thank you for taking me under your wing and teaching me about perovskites, scientific writing and data representation. Andoria, thank you for introducing me to the lab and teaching me the ropes. Thank you for the two excellent beam times we have had together and for teaching me to dress for success! Thank you, Charlotte, for teaching me how to manufacture titania nanotube electrodes and for sharing your passion for them. Thank you, Yu-Chuan, for always being up to help people, both at work and after work. I appreciate your help with ICI and EIS measurements and discussions as well as your impeccable music taste. Tove, thank you for the FlexPES measurements and all the help with the XAS analysis.

Thank you, everybody in the lab and fika table, who contributed to making this place a pleasant working environment: Agnes, Ahmed, Alexandra, Alex B, Alina, Alma, Anastasiia, Anders, Andreas, Andoria, Andy, Aram, Ashok, Babsi, Bojana, Burak, Casimir, Cesar, Charlotte, Christofer, Cuc, Daniel A, Daniel B, Daniel F, Dennis, Djurdjija, Dickson, Edvin, Erik Berg, Erik Björklund, Erik L, Florian, Fredrik B, Fredrik L, Funeka, Gaole, Girish, Gunnar, Gustav, Haidong, Harish, Heyin, Ida N, Ida Å, Igancio, Isabell, Jackie, Jeff, Johan C, Johan G, John, Jonas H, Jonas M, Jonas W, Jonas Å, Jorge, Katalin, Kenza, Killian, Kristina E, Kristina v F, Le Anh, Leif N, Leif E, Leidan, León, Litao, Luca, Luis, Maria H, Maria P, Mario, Markus (MEEEEK!), Martin,

Mats, Matt, Melania, Mikael A, Mikael O, Ming, Muchaha, Muchachita, Nataliia, Neeha, Ocean, Olle, Pedro, Peter, Pushpaka, Rebecca, Rebecka, Rassmus, Reza, Ritambhara, Robin, Rodrigo, Ronan, Ronnie, Saravanan, Sarmad (kreeeeeem!), Sebastian, Simon C, Simon L, Simon T, Sofia, Sophia, Souzan, Stefan, Tamara, Therese, Tim N, Tim M, Tristan, Tove, Ulf, Veronica, Vidyanand, Viktor F R, Viktor N, Victor P, Ville, Vitalii, Wandi, Wessel, Will, Yu-Chin, Yu-Chuan, Yu-Kai, Yonas, Zack and all I may have forgotten to name here.

Thank you, Andy, for our beamtimes in the UK and for answering your best on my endless questions about XPS. I have learnt how demanding it could be to be an XPS responsible, thank you so much for doing it.

Thank you, Yu-Kai, for your help with the SEM measurements.

Thanks, Funeka, for helping me with the conductivity measurements.

Thank you, Henrik, Rikard, Håkan, Long, Alina and Fredrik, for keeping our labs in order, especially Alina and Fredrik for coping with us for so long and solving the Argon and Ventilation Crisises.

I would also like to say thank you to Camilla, Lina, Eva, Martina and Isabel for all of the provided help with the administrative things, like my endless residence permits and visa letters.

I am exceptionally grateful for all the great people that I met at the department and who have become my real friends. Thank you ÅA club for always being there for me.

I would like to say a word of gratitude to Therese for organising absolutely best parties I have been to in Uppsala and its surroundings and also for cat-sitting our Sillen.

Thank you, Babsi, for being down for various outside-of-work activities to which, for example, Gustav would say no or which we have had even before I met him. Alles Leiwand!

Simon C, Therese, Gustav, Ville – thank you for teaching me extremely useful Swedish phrases and submerging me into Swedish culture.

Victor Pacheco – thank you for all the nice discussions on investments and TV shows that we have had. I hope you are enjoying your post PhD life in Örebro and will soon be fluent in Swedish.

Thank you, the jungle room, for being such great officemates: Robin, Yonas, Isabell and León. I am grateful for your ability to discuss our PhD studies and support my complaints about how tough PhD life could be. So sad that our office could not live up to its name.

I would like to reach out to the MaMaSELF community and say that I am grateful to be part of it. Without obtaining the MaMaSELF master's degree I would probably have never got this PhD position.

Last but not least, I would like to thank my family for all the support they gave me during this journey.

Спасибо, родители, за счастливое детство и за то, что отдали меня в семнадцатую школу. Спасибо моим сёстрам, что вы всегда знаете мои

шутки и готовы путешествовать со мной в разные уголки мира (зубы и путешествия)!

Спасибо моим бабушке и дедушке, за то, что вы всегда интересуетесь, как у меня дела и всегда ждёте в Доскино в баньку и на жареную картошку!

I would now like to thank the Eks family: Niklas, Gustav, Sara and Simon. Thank you for all the family celebrations I have had a chance to be part of and all the warmth you have shared with me.

And finally, to my significant other, Gustav: thank you for always being so supportive and reminding me that life is often easier than I sometimes think about it. Meeting you is truly the greatest thing that has happened to me in Sweden, jag älskar dig av hela mitt hjärta <3.

Bibliography

1. United Nations / Framework Convention on Climate Change (2015) Adoption of the Paris Agreement, 21st Conference of the Parties, Paris: United Nations. AN OFFICIAL PUBLICATION.

2. Dincer, I. Energy and Environmental impacts: Present and Future Perspectives. *Energy Sources* **20,** 427–453 (1998).

3. Dincer, I. Renewable energy and sustainable development: A crucial review. *Renewable & sustainable energy reviews sustainable energy reviews* **4,** 157–175 (2000).

4. O'Sullivan, M., Overland, I. & Sandalow, D. The Geopolitics of Renewable Energy. *SSRN Electronic Journal* (2017).

5. Dunn, B., Kamath, H. & Tarascon, J. M. Electrical energy storage for the grid: A battery of choices. *Science* **334,** 928–935 (2011).

6. Chu, S. & Majumdar, A. Opportunities and challenges for a sustainable energy future. *Nature* **488,** 294–303 (2012).

7. NobelPrize.org. *The Nobel Prize in Chemistry 2019.* `https://www.nobelprize.org/prizes/chemistry/2019/summary/`. Nobel Prize Outreach AB, 2023. Accessed: 2023-01-09.

8. Etacheri, V., Marom, R., Elazari, R., Salitra, G. & Aurbach, D. Challenges in the development of advanced Li-ion batteries: A review. *Energy and Environmental Science* **4,** 3243–3262 (2011).

9. Bradley, D. Building better batteries. *Education in Chemistry* **47,** 124–125 (2010).

10. Goodenough, J. B. & Kim, Y. Challenges for rechargeable Li batteries. *Chemistry of Materials* **22,** 587–603 (2010).

11. Kurzweil, P. & Brandt, K. *Overview of rechargeable lithium battery systems* 47–82 (Elsevier B.V., 2018).

12. *IUPAC. Compendium of Chemical Terminology (The "Gold Book")* 2nd (ed McNaught, A. D. and A. Wilkinson., A.) (Blackwell Scientific Publications, Oxford, 1997).

13. Billaud, D., Henry, F. X., Lelaurain, M. & Willmann, P. Revisited structures of dense and dilute stage II lithium-graphite intercalation compounds. *Journal of Physics and Chemistry of Solids* **57,** 775–781 (1996).

14. Billaud, D. & Henry, F. X. Structural studies of the stage III lithium – graphite intercalation compound. *Solid State Communications* **124,** 299–304 (2002).

15. Dahn, J. Phase diagram of LixC6. *Physical Review B* **44,** 9170–9177 (1991).

16. Wang, W. *et al.* Advances of TiO2 as Negative Electrode Materials for Sodium-Ion Batteries. *Advanced Materials Technologies* **3,** 1800004 (2018).

17. Borghols, W. J. H. *et al.* Lithium Storage in Amorphous TiO2 Nanoparticles. *Journal of The Electrochemical Society* **157,** A582–A588 (2010).

18. Kavan, L. Lithium insertion into TiO2 (anatase): Electrochemistry, Raman spectroscopy, and isotope labeling. *Journal of Solid State Electrochemistry* **18,** 2297–2306 (2014).

19. Sandhya, C. P., John, B. & Gouri, C. Lithium titanate as anode material for lithium-ion cells: A review. *Ionics* **20,** 601–620 (2014).

20. Yu, S. H., Feng, X., Zhang, N., Seok, J. & Abruña, H. D. Understanding Conversion-Type Electrodes for Lithium Rechargeable Batteries. *Accounts of Chemical Research* **51,** 273–281 (2018).

21. Klein, F. *et al.* Reaction mechanism and surface film formation of conversion materials for lithium- and sodium-ion batteries: An XPS case study on sputtered copper oxide (CuO) thin film model electrodes. *Journal of Physical Chemistry C* **120,** 1400–1414 (2016).

22. Böhme, S., Edström, K. & Nyholm, L. Overlapping and rate controlling electrochemical reactions for tin(IV) oxide electrodes in lithium-ion batteries. *Journal of Electroanalytical Chemistry* **797,** 47–60 (2017).

23. Goriparti, S. *et al.* Review on recent progress of nanostructured anode materials for Li-ion batteries. *Journal of Power Sources* **257,** 421–443 (2014).

24. McDowell, M. T., Lee, S. W., Nix, W. D. & Cui, Y. 25th anniversary article: Understanding the lithiation of silicon and other alloying anodes for lithium-ion batteries. *Advanced Materials* **25,** 4966–4985 (2013).

25. Rehnlund, D. *et al.* Lithium trapping in alloy forming electrodes and current collectors for lithium based batteries. *Energy and Environmental Science* **10,** 1350–1357 (2017).

26. Lindgren, F. *et al.* On the Capacity Losses Seen for Optimized Nano-Si Composite Electrodes in Li-Metal Half-Cells. *Advanced Energy Materials* **9** (2019).

27. Barsoum, M. W. *MAX phases: properties of machinable ternary carbides and nitrides* 1–708 (Wiley-VCH Verlag GmbH Co. KGaA, Weinheim, Germany, 2013).

28. Medkour, Y., Roumili, A., Maouche, D. & Louail, L. *Electrical properties of MAX phases* 159–175 (Woodhead Publishing Limited, 2012).

29. Eklund, P., Beckers, M., Jansson, U., Högberg, H. & Hultman, L. The Mn + 1AXn phases: Materials science and thin-film processing. *Thin Solid Films* **518,** 1851–1878 (2010).

30. Falcone, A. *The many facets of MXenes* https://exelmagazine.org/article/the-many-facets-of-mxenes. Drexel university research magazine, 2012. Accessed: 2023-01-05.

31. Naguib, M. *et al.* Two-dimensional nanocrystals produced by exfoliation of Ti 3AlC 2. *Advanced Materials* **23,** 4248–4253 (2011).

32. Gonzalez-Julian, J. Processing of MAX phases: From synthesis to applications. *Journal of the American Ceramic Society* **104,** 659–690 (2021).

33. Anasori, B. *et al.* Two-Dimensional, Ordered, Double Transition Metals Carbides (MXenes). *ACS Nano* **9,** 9507–9516 (2015).

34. Gogotsi, Y. & Anasori, B. The Rise of MXenes. *ACS Nano* **13,** 8491–8494 (2019).

35. Rasool, K. *et al.* Antibacterial Activity of Ti3C2Tx MXene. *ACS Nano* **10,** 3674–3684 (2016).

36. Unal, M. A. *et al.* 2D MXenes with antiviral and immunomodulatory properties: A pilot study against SARS-CoV-2. *Nano Today* **38,** 101136 (2021).

37. Panda, S., Deshmukh, K., Mustansar Hussain, C. & Khadheer Pasha, S. K. 2D MXenes for combatting COVID-19 Pandemic: A perspective on latest developments and innovations. *FlatChem* **33,** 100377 (2022).

38. Naguib, M. *et al.* MXene: A promising transition metal carbide anode for lithium-ion batteries. *Electrochemistry Communications* **16,** 61–64 (2012).

39. Mashtalir, O. *et al.* Intercalation and delamination of layered carbides and carbonitrides. *Nature Communications* **4:1716** (2013).

40. Naguib, M. *et al.* New two-dimensional niobium and vanadium carbides as promising materials for li-ion batteries. *Journal of the American Chemical Society* **135,** 15966–15969 (2013).

41. Kajiyama, S. *et al.* Sodium-Ion Intercalation Mechanism in MXene Nanosheets. *ACS Nano* **10,** 3334–3341 (2016).

42. Gentile, A. *et al.* Enhanced Functional Properties of Ti3C2Tx MXenes as Negative Electrodes in Sodium-Ion Batteries by Chemical Tuning. *Small Methods* **4,** 1–13 (2020).

43. Bak, S. M. *et al.* Na-Ion Intercalation and Charge Storage Mechanism in 2D Vanadium Carbide. *Advanced Energy Materials* **7,** 1700959 (2017).

44. Dong, Y. *et al.* Ti3C2 MXene-Derived Sodium/Potassium Titanate Nano-ribbons for High-Performance Sodium/Potassium Ion Batteries with Enhanced Capacities. *ACS Nano* **11,** 4792–4800 (2017).

45. Er, D., Li, J., Naguib, M., Gogotsi, Y. & Shenoy, V. B. Ti3C2 MXene as a High Capacity Electrode Material for Metal (Li, Na, K, Ca) Ion Batteries. *ACS Applied Materials and Interfaces* **6,** 11173–11179 (2014).

46. Naguib, M. *et al.* Electrochemical performance of MXenes as K-ion battery anodes. *Chemical Communications* **53,** 6883–6886 (2017).

47. Kaland, H. *et al.* Are MXenes suitable as cathode materials for rechargeable Mg batteries? *Sustainable Energy and Fuels* **4,** 2956–2966 (2020).

48. Zhao, M. Q. *et al.* Magnesium-Ion Storage Capability of MXenes. *ACS Applied Energy Materials* **2,** 1572–1578 (2019).

49. Rao, Q.-s., Liao, S.-y., Huang, X.-w., Li, Y.-z. & Liu, Y.-d. Assembly of MXene/PP Separator and Its Enhancement for Ni-Rich LiNi0.8Co0.1Mn0.1O2 Electrochemical Performance. *Polymers* **12,** 2192 (2020).

50. Likitaporn, C. *et al.* High electrolyte uptake of MXene integrated membrane separators for Zn-ion batteries. *Scientific Reports* **12,** 1–13 (2022).

51. Kaland, H. *et al.* Performance Study of MXene/Carbon Nanotube Composites for Current Collector- and Binder-Free Mg–S Batteries. *ChemSusChem* **14,** 1864–1873 (2021).

52. Wang, C. H. *et al.* Titanium Carbide (MXene) as a Current Collector for Lithium-Ion Batteries. *ACS Omega* **3,** 12489–12494 (2018).

53. Ghidiu, M., Lukatskaya, M. R., Zhao, M. Q., Gogotsi, Y. & Barsoum, M. W. Conductive two-dimensional titanium carbide 'clay' with high volumetric capacitance. *Nature* **516,** 78–81 (2015).

54. Lukatskaya, M. R. *et al.* Cation Intercalation and High Volumetric Capacitance of Two-Dimensional Titanium Carbide. *Science* **341,** 1502–1505 (2013).

55. Lukatskaya, M. R. *et al.* Probing the Mechanism of High Capacitance in 2D Titanium Carbide Using in Situ X-Ray Absorption Spectroscopy. *Advanced Energy Materials* **5,** 2–5 (2015).

56. Dall'Agnese, Y., Rozier, P., Taberna, P. L., Gogotsi, Y. & Simon, P. Capacitance of two-dimensional titanium carbide (MXene) and MXene/carbon nanotube composites in organic electrolytes. *Journal of Power Sources* **306,** 510–515 (2016).

57. Halim, J. *et al.* Tailored synthesis approach of (Mo2/3Y1/3)2AlC: I - MAX and its two-dimensional derivative Mo1.33CTzMXene: Enhancing the yield, quality, and performance in supercapacitor applications. *Nanoscale* **13,** 311–319 (2021).

58. Zhu, C. & Geng, F. Macroscopic MXene ribbon with oriented sheet stacking for high-performance flexible supercapacitors. *Carbon Energy* **3,** 142–152 (2021).

59. Morales-Garciá, Á., Calle-Vallejo, F. & Illas, F. MXenes: New Horizons in Catalysis. *ACS Catalysis* **10,** 13487–13503 (2020).

60. Wang, L. *et al.* MXenes as Heterogeneous Fenton-like Catalysts for Removal of Organic Pollutants: A Review. *Journal of Environmental Chemical Engineering* **10,** 108954 (2022).

61. Peera, S. G. *et al.* 2D MXene Nanomaterials as Electrocatalysts for Hydrogen Evolution Reaction (HER): A Review. *Micromachines* **13,** 1–34 (2022).

62. Sarycheva, A. *et al.* 2D titanium carbide (MXene) for wireless communication. *Science Advances* **4,** 1–9 (2018).

63. Han, M. *et al.* Solution-Processed Ti3C2Tx MXene Antennas for Radio-Frequency Communication. *Advanced Materials* **33,** 1–7 (2021).

64. Alhabeb, M. *et al.* Guidelines for Synthesis and Processing of Two-Dimensional Titanium Carbide (Ti3C2Tx MXene). *Chemistry of Materials* **29,** 7633–7644 (2017).

65. Zhang, T. *et al.* Synthesis of two-dimensional Ti3C2TxMXene using HCl+LiF etchant: Enhanced exfoliation and delamination. *Journal of Alloys and Compounds* **695,** 818–826 (2017).

66. Kurra, N. *et al.* Bistacked Titanium Carbide (MXene) Anodes for Hybrid Sodium-Ion Capacitors. *ACS Energy Letters* **3,** 2094–2100 (2018).

67. Anayee, M. *et al.* Role of acid mixtures etching on the surface chemistry and sodium ion storage in Ti3C2TxMXene. *Chemical Communications* **56,** 6090–6093 (2020).

68. Sang, X. *et al.* Atomic defects in monolayer titanium carbide (Ti3C2Tx) MXene. *ACS Nano* **10,** 9193–9200 (2016).

69. Li, T. *et al.* Fluorine-Free Synthesis of High-Purity Ti3C2Tx (T=OH, O) via Alkali Treatment. *Angewandte Chemie - International Edition* **57,** 6115–6119 (2018).

70. Yang, S. *et al.* Fluoride-Free Synthesis of Two-Dimensional Titanium Carbide (MXene) Using A Binary Aqueous System. *Angewandte Chemie* **130,** 15717–15721 (2018).

71. Natu, V. *et al.* 2D Ti3C2Tz MXene Synthesized by Water-free Etching of Ti3AlC2 in Polar Organic Solvents. *Chem* **6,** 616–630 (2020).

72. Li, M. *et al.* Element Replacement Approach by Reaction with Lewis Acidic Molten Salts to Synthesize Nanolaminated MAX Phases and MXenes. *Journal of the American Chemical Society* **141,** 4730–4737. arXiv: `1901.05120` (2019).

73. Li, Y. *et al.* A general Lewis acidic etching route for preparing MXenes with enhanced electrochemical performance in non-aqueous electrolyte. *Nature Materials* **19,** 894–899 (2020).

74. Mohammadi, A. V., Rosen, J. & Gogotsi, Y. The world of two-dimensional carbides and nitrides (MXenes). *Science* **372,** eabf1581 (2021).

75. Ren, C. E. *et al.* Porous Two-Dimensional Transition Metal Carbide (MXene) Flakes for High-Performance Li-Ion Storage. *ChemElectroChem* **3,** 689–693 (2016).

76. Wu, Y. *et al.* Exploring MXene-based materials for next-generation rechargeable batteries. *Journal of Physics: Energy* **3,** 032009 (2021).

77. Liu, S. *et al.* Ti 3 C 2 T x MXenes-based flexible materials for electrochemical energy storage and solar energy conversion. *Nanophotonics* **11,** 3215–3245 (2022).

78. Sahoo, S. K., Manoharan, B. & Sivakumar, N. in *Perovskite Photovoltaics: Basic to Advanced Concepts and Implementation* 1–24 (Academic Press, Cambridge, MA, USA, 2018).

79. Madshus, I. H. & Olsnes, S. Selective inhibition of sodium-linked and sodium-independent bicarbonate/chloride antiport in Vero cells. *Journal of Biological Chemistry* **262,** 7486–7491 (1987).

80. Ibarra, J. *et al.* Influence of composition on the structure and conductivity of the fast ionic conductors La2/3-xLi3xTiO3 (0.03≤x≤0.167). *Solid State Ionics* **134,** 219–228 (2000).

81. Belous, A. G., Novitskaya, G. N., Polyanetskaya, S. V. & Gornikov, Y. I. Investigation into complex oxides of La2/3-xLi3xTiO3 composition. *Izvestiia Akademii nauk SSSR. Neorganicheskie materialy.* **23,** 470–472 (1987).

82. Inaguma, Y., Chen, L., Itoh, M. & Nakamura, T. High lithium ion conductivity in the perovskite-type compounds. *Solid State Communications* **86,** 689–693 (1993).

83. Inaguma, Y., Chen, L., Itoh, M. & Nakamura, T. Candidate compounds with perovskite structure for high lithium ionic conductivity. *Solid State Ionics* **70-71,** 196–202 (1994).

84. Birke, P., Scharner, S., Huggins, R. A. & Weppner, W. Electrolytic Stability Limit and Rapid Lithium Insertion in the Fast-Ion-Conducting Li0.29La0.57TiO3 Perovskite-Type Compound. *Journal of The Electrochemical Society* **144,** L167–L169 (1997).

85. Chen, C. H. & Amine, K. Ionic conductivity, lithium insertion and extraction of lanthanum lithium titanate. *Solid State Ionics* **144,** 51–57 (2001).

86. Amores, M. *et al.* Li1.5La1.5MO6 (M = W6+, Te6+) as a new series of lithium-rich double perovskites for all-solid-state lithium-ion batteries. *Nature Communications* **11,** 1–12 (2020).

87. Zhang, L. *et al.* Lithium lanthanum titanate perovskite as an anode for lithium ion batteries. *Nature Communications* **11,** 1–8 (2020).

88. Inaguma, Y. *et al.* Effect of substitution and pressure on lithium ion conductivity in perovskites Ln1/2Li1/2TiO3 (Ln = La, Pr, Nd and Sm). *Journal of Physics and Chemistry of Solids* **58,** 843–852 (1997).

89. Latie, L., Villeneuve, G., Conte, D. & Le Flem, G. Ionic conductivity of oxides with general formula LixLn1/3Nb1-xTixO3 (Ln = La, Nd). *Journal of Solid State Chemistry* **51,** 293–299 (1984).

90. Chung, H. T., Kim, J. G. & Kim, H. G. Dependence of the lithium ionic conductivity on the B-site ion substitution in (Li0.5La0.5)Ti1-xMxO3 (M = Sn, Zr, Mn, Ge). *Solid State Ionics* **107,** 153–160 (1998).

91. Thangadurai, V. & Weppner, W. Effect of B-site substitution of (Li,La)TiO3 perovskites by Di-, tri-, tetra- and hexavalent metal ions on the lithium ion conductivity. *Ionics* **6,** 70–77 (2000).

92. Yashima, M., Itoh, M., Inaguma, Y. & Morii, Y. Crystal structure and diffusion path in the fast lithium-ion conductor La0.62Li0.16TiO3. *Journal of the American Chemical Society* **127,** 3491–3495 (2005).

93. Rivera, A. *et al.* Percolation-Limited Ionic Diffusion in Li0.5-xNaxLa0.5TiO3 Perovskites (0 ≤ x ≤ 0.5). *Chem. Mater* **14,** 5148–5152 (2002).

94. Bucheli, W. *et al.* Near constant loss regime in fast ionic conductors analyzed by impedance and NMR spectroscopies. *Physical Chemistry Chemical Physics* **16,** 15346–15354 (2014).

95. Alonso, J. A. *et al.* On the Location of Li+ Cations in the fast Li-Cation Conductor La0.5Li0.5TiO3 Perovskite. *Angewandte Chemie - International Edition* **39,** 619–621 (2000).

96. Inaguma, Y., Katsumata, T. & Itoh. Lithium lon Conductivity in A-site Deficient Perovskites Sr0.55La0.05Li0.35□0.1Ti0.5Ta0.50O3 and Sr0.35La0.15Li0.35□0.15ITi0.5Ta0.5O3. *Electrochemistry* **68,** 534–536 (2000).

97. Brant, W. R. *et al.* Rapid lithium insertion and location of mobile lithium in the defect perovskite Li0.18Sr0.66Ti0.5Nb0.5O3. *ChemPhysChem* **13,** 2293–2296 (2012).

98. Brant, W. R. *et al.* Temperature and composition dependent structural investigation of the defect perovskite series Sr1-xTi1-2xNb2xO 3, 0≤x≤0.2. *Journal of Solid State Chemistry* **183,** 1998–2003 (2010).

99. Etman, A. S., Halim, J. & Rosen, J. Mixed MXenes: Mo1.33CTz and Ti3C2Tz freestanding composite films for energy storage. *Nano Energy* **88,** 106271 (2021).

100. Wei, W. *et al.* High energy and power density TiO2 nanotube electrodes for 3D Li-ion microbatteries. *Journal of Materials Chemistry A* **1,** 8160–8169 (2013).

101. Wei, W., Valvo, M., Edström, K. & Nyholm, L. Size-Dependent Electrochemical Performance of Monolithic Anatase TiO2 Nanotube Anodes for Sodium-Ion Batteries. *ChemElectroChem* **5,** 674–684 (2018).

102. Wei, W., Ihrfors, C., Björefors, F. & Nyholm, L. Capacity Limiting Effects for Freestanding, Monolithic TiO2 Nanotube Electrodes with High Mass Loadings. *ACS Applied Energy Materials* **3,** 4638–4649 (2020).

103. Seisenbaeva, G. A., Daniel, G., Nedelec, J.-M., Gun'ko, Y. K. & Kessler, V. G. High surface area ordered mesoporous nano-titania by a rapid surfactant-free approach. *Journal of Materials Chemistry* **22,** 20374–20380 (2012).

104. Lacey, M. J. Influence of the Electrolyte on the Internal Resistance of Lithium−Sulfur Batteries Studied with an Intermittent Current Interruption Method. *ChemElectroChem* **4,** 1997–2004 (2017).

105. Chien, Y. C., Menon, A. S., Brant, W. R., Brandell, D. & Lacey, M. J. Simultaneous Monitoring of Crystalline Active Materials and Resistance Evolution in Lithium-Sulfur Batteries. *Journal of the American Chemical Society* **142,** 1449–1456 (2020).

106. Chien, Y.-C. *et al.* A fast alternative to the galvanostatic intermittent titration technique. *ChemRxiv* (2021).

107. Abbate, M. *et al.* Probing Depth of Soft X-ray Absorption Spectroscopy Measured in Total-Electron-Yield Mode. *Surface and Interface Analysis* **18,** 65–69 (1992).

108. Frazer, B. H., Gilbert, B., Sonderegger, B. R. & De Stasio, G. The probing depth of total electron yield in the sub-keV range: TEY-XAS and X-PEEM. *Surface Science* **537,** 161–167 (2003).

109. Asakura, D. *et al.* Material/element-dependent fluorescence-yield modes on soft X-ray absorption spectroscopy of cathode materials for Li-ion batteries. *AIP Advances* **6,** 035105 (2016).

110. Seah, M. P. & Dench, W. A. Quantitative Electron Spectroscopy of Surfaces : A Standard Data Base for Electron Inelastic Mean Free Path in Solids. *Surface and Interface Analysis* **1,** 2–11 (1979).

111. Fairely, N. *CasaXPS Manual 2.3. 15 Getting started with CasaXPS* 1–177 (Casa Software Ltd, Teignmouth, Devon, UK, 2009).

112. Ravel, B. & Newville, M. ATHENA, ARTEMIS, HEPHAESTUS: Data analysis for X-ray absorption spectroscopy using IFEFFIT. *Journal of Synchrotron Radiation* **12,** 537–541 (2005).

113. Tang, Q., Zhou, Z. & Shen, P. Are MXenes promising anode materials for Li ion batteries? Computational studies on electronic properties and Li storage capability of Ti 3C 2 and Ti 3C 2X 2 (X = F, OH) monolayer. *Journal of the American Chemical Society* **134,** 16909–16916 (2012).

114. Halim, J. *et al.* X-ray photoelectron spectroscopy of select multi-layered transition metal carbides (MXenes). *Applied Surface Science* **362,** 406–417 (2016).

115. Persson, I. *et al.* On the organization and thermal behavior of functional groups on Ti3C2 MXene surfaces in vacuum. *2D Materials* **5,** 015002 (2018).

116. Xie, Y. *et al.* Role of surface structure on li-ion energy storage capacity of two-dimensional transition-metal carbides. *Journal of the American Chemical Society* **136,** 6385–6394 (2014).

117. Xie, Y. *et al.* Prediction and Characterization of MXene Nanosheet Anodes for Non-Lithium-Ion Batteries. *ACS Nano* **8,** 9606–9615 (2014).

118. Kajiyama, S. *et al.* Sodium-Ion Intercalation Mechanism in MXene Nanosheets. *ACS Nano* **10,** 3334–3341 (2016).

119. Wang, X. *et al.* Atomic-Scale Recognition of Surface Structure and Intercalation Mechanism of Ti3C2X. *Journal of the American Chemical Society* **137,** 2715–2721 (2015).

120. Bärmann, P., Winter, M., Gonzalez-Julian, J. & Placke, T. Solvent Co-Intercalation-Induced Activation and Capacity Fade Mechanism of Few-/Multi-Layered MXenes in Lithium Ion Batteries. *Small* **17,** 2104130 (2021).

121. Zhang, C. J. *et al.* Oxidation Stability of Colloidal Two-Dimensional Titanium Carbides (MXenes). *Chemistry of Materials* **29,** 4848–4856 (2017).

122. Cao, M. *et al.* Room Temperature Oxidation of Ti 3 C 2 MXene for Supercapacitor Electrodes. *Journal of The Electrochemical Society* **164,** A3933–A3942 (2017).

123. Huang, S. & Mochalin, V. N. Hydrolysis of 2D Transition-Metal Carbides (MXenes) in Colloidal Solutions. *Inorganic Chemistry* **58,** 1958–1966 (2019).

124. Chen, Z., Belharouak, I., Sun, Y. K. & Amine, K. Titanium-based anode materials for safe lithium-ion batteries. *Advanced Functional Materials* **23,** 959–969 (2013).

125. Shpigel, N. *et al.* Direct Assessment of Nanoconfined Water in 2D Ti 3 C 2 Electrode Interspaces by a Surface Acoustic Technique. *Journal of the American Chemical Society* **140,** 8910–8917 (2018).

126. Kong, F. *et al.* Improving the electrochemical properties of MXene Ti3C2 multilayer for Li-ion batteries by vacuum calcination. *Electrochimica Acta* **265,** 140–150 (2018).

127. Fagerli, F. H. *et al.* Removing Fluoride-Terminations from Multilayered V2C TxMXene by Gas Hydrolyzation. *ACS Omega* **7,** 23790–23799 (2022).

128. Asfaw, H. D., Tai, C. W., Nyholm, L. & Edström, K. Over-Stoichiometric NbO2 Nanoparticles for a High Energy and Power Density Lithium Microbattery. *ChemNanoMat* **3,** 646–655 (2017).

129. Catti, M. & Ghaani, M. R. On the lithiation reaction of niobium oxide: Structural and electronic properties of Li1.714Nb2O5. *Physical Chemistry Chemical Physics* **16,** 1385–1392 (2014).

130. Kumagai, N., Koishikawa, Y., Komaba, S. & Koshiba, N. Electrochemical Kinetics of Lithium Intercalation into Nb2O5 Electrodes for a 2 V Rechargeable Lithium Battery. *Journal of The Electrochemical Society* **146,** 3203–3210 (1999).

131. Nadiri, A., Le Flem, G. & Delmas, C. Lithium intercalation in Ln1/3NbO3 perovskite-type phases (Ln = La, Nd). *Journal of Solid State Chemistry* **73,** 338–347 (1988).

132. Zhang, L. *et al.* Lithium lanthanum titanate perovskite as an anode for lithium ion batteries. *Nature Communications* **11,** 1–8 (2020).

133. Shan, Y. J., Chen, L., Inaguma, Y., Itoh, M. & Nakamura, T. Oxide cathode with perovskite structure for rechargeable lithium batteries. *Journal of Power Sources* **54,** 397–402 (1995).

134. García-Alvarado, F., Várez, A., Morán, E. & Alario-Franco, M. A. Structural details and lithium intercalation in the perovskite La0.5Li0.5TiO3. *Phase Transitions* **58,** 111–120 (1996).

135. Brant, W. R., Li, D., Gu, Q. & Schmid, S. Comparative analysis of ex-situ and operando X-ray diffraction experiments for lithium insertion materials. *Journal of Power Sources* **302,** 126–134 (2016).

136. Brant, W. R. *et al.* A large format in operando wound cell for analysing the structural dynamics of lithium insertion materials. *Journal of Power Sources* **336,** 279–285 (2016).

Acta Universitatis Upsaliensis

Digital Comprehensive Summaries of Uppsala Dissertations
from the Faculty of Science and Technology 2257

Editor: The Dean of the Faculty of Science and Technology